Acta Astronautica 231 (2025) 246–267

Contents lists available at ScienceDirect

Acta Astronautica

journal homepage: www.elsevier.com/locate/actaastro

Systematic methodology for the preliminary design of future rotary VTOL Martian aerobots

Vishal Youhanna *, Leonard Felicetti, Dmitry Ignatyev

Faculty of Engineering and Applied Sciences, Cranfield University, College Rd, Cranfield, Bedford, MK43 0AL, UK

ARTICLE INFO

Keywords:
Mars exploration
Martian drone framework
Planetary aerobots
Rotorcraft conceptual design
UAV

ABSTRACT

This paper proposes and describes a methodology for the preliminary design of aerobots for future Martian exploration missions within a framework. The methodology takes into account inputs derived from top-level mission requirements and site locations to obtain the critical mission parameters that affect the performance of the rotorcraft. The proposed methodology allows for incorporating multi-rotor configurations into the trade-offs based on the required power to perform flight profiles. The equations, based on momentum theory for conventional helicopters, are derived and generalised to estimate the required power for flight segments such as hover, vertical climb, and forward flight for rotorcraft with both overlapping and non-overlapping rotors such as coaxial, tandem, and multirotor configurations. The resulting performance data is used for sizing and selecting the critical components of the aerobot in a mission scenario, such as rotor and battery sizes. Notably, the analyses conducted on rotorcraft with single and dual rotors identified a tandem rotorcraft configuration without folding mechanisms as the optimal choice due to its superior power efficiency and mechanical simplicity. Through calculated equations for battery mass and available empty mass estimation, this framework enables the optimisation and selection of an efficient rotary VTOL aerobot for Martian missions in the years to come.

1. Introduction

The predominant approach to in-situ exploration of Mars has historically relied on landers and rovers, but their limitations have sparked interest in designing specialised aerial robots known as aerobots. The concept of unmanned aerial vehicles has gained prominence due to their advantages over surface rovers, including increased speed, broader range, obstacle avoidance capabilities, and improved visibility [1]. While chronological planetary exploration mainly explored the use of lighter-than-air airships or fixed-wing planes, recent advancements in drone technology have rekindled interest in rotorcraft for Mars exploration. These technological advancements culminated in the successful deployment of the first operational aerobot on Mars by NASA's Ingenuity Mars Helicopter. The vehicle, having landed on Mars in February 2021, completed 72 short autonomous pre-commanded flights before retiring in January 2024, accumulating approximately 129 min of flight time, covering 17 km, reaching altitudes of up to 24 m, and achieving ground speeds of up to 10 m/s [2]. These flight tests marked the transition of Ingenuity from the Technology Demonstration phase to the Operations Demonstration phase, demonstrating the potential for collaboration between future rovers and aerial surveyors [2]. The insights gained from designing and operating the Mars Helicopter offer valuable knowledge for developing advanced aerobots for Mars exploration.

1.1. Martian flight conditions

The unique features of Mars pose challenges for rotorcraft design, primarily due to its atmospheric conditions. Despite the lower gravity of Mars, its average atmospheric density is approximately 100 times lower than that of Earth [3], leading to a very low Reynolds number during rotor operations, especially for small-scale helicopters. However, the Mach number on Mars would be significantly higher due to two main factors: the necessity for higher tip speeds to compensate for the lower atmospheric density, and the reduced speed of sound on the Martian surface, which is only about 70% of that on Earth. These conditions significantly constrain the rotorcraft design [4]. Another challenge in sustaining the flight of Martian drones involves managing the heat generated by the propulsion system while generating the required lift. This task is exceptionally demanding given the low Reynolds number

* Corresponding author.
E-mail address: vishal.youhanna@cranfield.ac.uk (V. Youhanna).

https://doi.org/10.1016/j.actaastro.2025.01.059
Received 29 July 2024; Received in revised form 22 December 2024; Accepted 24 January 2025
Available online 25 January 2025
0094-5765/© 2025 The Authors. Published by Elsevier Ltd on behalf of IAA. This is an open access article under the CC BY license (http://creativecommons.org/licenses/by/4.0/).

involved. Furthermore, the size constraint set by an aeroshell required to transport the aerobot to Mars introduces additional complexities [5]. These factors have historically cast doubt on the feasibility of using rotating-wing aerobots on Mars, a scepticism dispelled by the first Mars Helicopter.

The success of Ingenuity, while groundbreaking, exposes the inherent limitations of small-sized, basic-configured aerobots on Mars. These constraints limit their ability to conduct expansive scientific missions that demand extended flights, larger payloads, advanced communication systems, or robust propulsion for high-altitude endeavours. Addressing these limitations necessitates reimagining the parameters of Martian aerobot missions. Enhancing the Ingenuity Helicopter could involve augmenting its size or integrating fixed wings into its configuration, aiming to extend endurance, and payload capacity and accommodate more solar panels.

1.2. Literature

Diverse proposals for Mars exploration have explored VTOL aircraft with rigid or adaptable body configurations [6–16]. The first rotary VTOL planetary aerial vehicle design concepts were pioneered by Young et al. (2000) [6], particularly advocating for a Mars tiltrotor as a balanced solution between hover performance and cruise range as both attributes are critical for Mars exploration. Y-4 Tilt-Rotor VTOL Aerobot [7], the fourth and final design iteration studied at the University of Surrey from 2004 to 2016, was such a concept that used two smaller tractor tiltrotors to provide the thrust needed for both vertical and horizontal flight, and a coaxial rotor embedded at the centre of the blended wing for VTOL. Whereas another configuration, called MIRAGE [8], used a fan embedded in the centre of the blended wing body (4.8 m wingspan) for VTOL and a propeller on the nose for forward thrust. Among these types of transitioning aircraft is the tailsitter configuration, which takes off and lands vertically on its tail, and for forward flight the whole body tilts horizontally in midair. Martian Twin Rotor Tailsitter design [9] and Mars Electric Reusable Flyer (MERF) [10] are dual-rotor VTOL tailsitter concepts proposed with a reusable option and foldable body, which when deployed would have a wingspan of 7.5 m and 0.9 m, respectively. VITAS [11] is another tailsitter concept with 4 coaxial rotors positioned at the tips of an x-wing configuration with a wingspan of about 2 m and is equipped with a canard for pitch control. Besides using vertical propulsion generated by rotary blades, there are concepts such as Mars Gashopper [12] and Marshopper [13], that propose to utilise local carbon dioxide to store and pressurise the gas inside the aircraft system and then propel it out to hop above the surface of Mars for VTOL. Both these designs are equipped with wings to glide around for increased endurance during forward flight. Among large foldable and small rigid fixed wing rotorcrafts, there is an inflatable wing concept that offers the advantage of transporting the aircraft to Mars in the limited aeroshell size. VALKERIE (Vertical-takeoff And Landing Kompact Electric Reusable Inflatable Explorer) [14] is such a design which merges the above-mentioned tailsitter MERF with BIGBLUE (Baseline Inflatable-wing Glider, Balloon-Launched Unmanned Experiment). BIGBLUE is an inflatable wing glider technology that was introduced and worked on by the students at the University of Kentucky for low air density environments such as Mars. The LILI (Long-term Ice-field Levitating Investigator) concept [15] further expands on foldable hybrid mobility by integrating a tandem rotor configuration with a ground-based sled system. This approach allows for efficient navigation of polar ice fields on Mars, leveraging the tandem rotors for aerial capability while optimising power use through surface mobility. NASA started developing the second generation of Mars Helicopters such as the Mars Science Helicopter (MSH) and Advanced Mars Helicopter (AMH), even before Ingenuity Helicopter had landed on Mars. MSH had two short-listed designs with foldable mechanisms and each weighed 20 kg, namely a coaxial rotorcraft with 2.5 m diameter rotors and a hexacopter design with 1.28 m diameter rotors [5], whereas AMH is a similar design to Ingenuity with 1.2 m diameter rotors but weighs 4.6 kg and is equipped with improved airfoils and science payload [16], on which attitude control and autonomous navigation are investigated in Ref. [17].

Among these concepts, the Valles Marineris Explorer (VaMEx) initiative evaluated coaxial helicopters and transition coaxial tailsitter configurations as part of a robotic swarm for Mars high ranges exploration [18]. For a mission with a 30 km cruise range and a 1.4 kg payload, the study shows that the 3.83 m wingspan transition tailsitter, while offering better cruise efficiency and enabling longer range through reduced battery weight, is outweighed by the added mass of its wings and stabilisers, resulting in a heavier and more complex design. In contrast, the coaxial helicopter, with 1.52 m rotors, is simpler, lighter, and more efficient, making it better suited for shorter missions. These findings highlight the need for comprehensive assessments to optimise rotorcraft designs for Martian conditions, particularly within aeroshell size constraints, assuming the stability of launch and re-entry technologies in the coming decades. Accommodating larger craft may require alternative solutions, such as separate transport, packaging with a smaller ground spacecraft, or innovative folding mechanisms within the aeroshell. However, aircraft design constraints imposed by practical aeroshell sizes are frequently disregarded in studies, particularly those not conducted by space agencies. For instance VaMEx study [18] defers the selection of aeroshell size and relative dimensions for future research and MIRAGE [8] proposed 5 m diameter aeroshell, which currently does not exist. Although the development of new aeroshells could provide greater flexibility, space missions prioritise established designs, such as the 4.5 m diameter aeroshells utilised in the Mars Science Laboratory (2011) and Mars 2020 missions, due to their proven reliability [5].

Previous studies in Martian rotorcraft design can be broadly classified into two categories: conceptual designs without feasibility validation and high-fidelity mission-specific studies. Conceptual studies often propose novel configurations, such as tiltrotors or hybrid rotorcraft models proposed in Ref. [4] and Coaxial Tri-rotor and Jumping Flying Aircraft concepts proposed in Ref. [19], but lack detailed analyses to quantify their practicality under Martian conditions. High-fidelity studies, while providing detailed performance evaluations, are computationally intensive and limited to predefined configurations. For instance, study such as in Ref. [20] used Blade Element Theory and experimental validation for quadrotor designs but do not generalise findings to other configurations. Similarly, studies on coaxial and transition vehicles for the Valles Marineris Explorer (VaMEx) [18] missions are modified to specific operational scenarios and do not extend to broader mission profiles. Multidisciplinary design frameworks, such as the one illustrated in Ref. [6], focus on vertical lift planetary aerial vehicles but emphasise spacecraft integration over rotorcraft design scalability.

1.3. Proposed research

This research introduces a scalable framework that combines the exploratory strengths of conceptual studies with the practicality of high-fidelity analyses. The framework integrates multidisciplinary design considerations, such as mission requirements, environmental constraints, and spacecraft integration, into a systematic process for preliminary rotorcraft design. A fundamentally novel aspect of this framework is its parametric analysis methodology, based on rotorcraft momentum theory, which enables rapid evaluation of power requirements, rotor sizing, and payload capacities for configurations such as single rotors and dual-rotor systems, including coaxial and tandem rotors. Although this paper focuses on these configurations, the methodology also applies to multirotor systems. This methodology integrates mission constraints, such as aeroshell size and power limitations, into a streamlined design process, making it inherently adaptable to varying planetary environments. By updating planetary parameters such as air density and gravitational acceleration, the framework can be applied to

other atmospheric environments, such as Titan [21] and Venus, making it a versatile tool for future exploration efforts. By simplifying aerodynamic analyses while maintaining computational efficiency, the framework accelerates decision-making and supports iterative design refinements. The performance outcomes, such as rotor and battery sizing, provide actionable insights for researchers and engineers, ensuring that the preliminary designs are grounded in theoretical rationale and aligned with mission requirements. Consequently, this approach addresses the limitations of small-sized aerobots while advancing scalable, mission-specific designs, paving the way for the next generation of Martian rotorcraft.

The structure of this research article is such that it begins with an overview (section 2) of the framework for preliminary Martian aerobot design methodology, a systematic approach on which the rest of the sections are constructed. This is succeeded by the development of a mission statement and requirements (section 3), and a definition of relative parameters (section 4). The outlined specifications and objectives highlight the complexity of Martian missions and the innovative strategies necessary to overcome challenges, providing insights into the potential outcomes of employing an aerobot in Mars exploration, and emphasising the advancements and challenges involved in planning and executing missions beyond Earth. A generalised methodology rooted in simplified momentum theory (section 5) is explained that enables the calculation of the required flight power of diverse Martian rotorcraft configurations, including overlapping rotors. Likewise, a methodology for the initial sizing of battery-electric aircraft (section 6) is introduced which inputs the flight required power to estimate the required battery mass and hence, provides insights into determining the total mass of the rotorcraft. After the description of the methodologies, study cases for parametric analysis are established (section 7) by forming a basic flight profile mission and locking necessary parameters to perform analysis on a single conventional helicopter, coaxial rotorcraft, and three created cases of tandem rotorcraft configurations. Subsequently, the results are demonstrated from the analysis performed (section 8) using the above-mentioned methodology to examine the relationship between rotor disk size and the power demands for hover, vertical climb, and forward flight across the selected rotorcraft configurations in the Martian environment. The insights from the rotorcraft power requirement analysis allow for the identification of the most power-efficient configurations for aerobot design. However, certain theoretical optima may introduce complexities due to design constraints, a factor pivotal in the selection and refinement of these configurations. Hence, based on this analytical approach the most suitable rotorcraft design is rationalised and shortlisted for the preliminary sizing (section 9).

2. Framework for preliminary Martian rotary VTOL aerobot design methodology

The flow chart in Fig. 1 illustrates the framework of the systematic methodology proposed and applied in this research for the preliminary design of future rotary VTOL Martian aerobots. The methodology is generalised with the aim of developing a rational case for the design of a Martian aerobot customised to a specific mission. Interplanetary space missions, given their complexities and one-shot nature with minimal margin for error, are inherently high-stakes operations. Any proposed advanced solution addressing current space exploration challenges must align with the existing state-of-the-art space infrastructure, as a mismatch could result in lengthy implementation timelines and render the solution obsolete before it can be deployed. Therefore, the first step in the framework is to identify the mission aim for the future aerobot, which should align with the priorities of global space agencies for upcoming Mars exploration missions. The second step is choosing a possible landing site that meets the engineering constraints and scientific goals and requirements set by the Mars scientific community. The next stage is to define the top-level mission profile for the operation of the aerobot. The subsequent step is to determine the flight operations and profile for the primary mission. Setting the performance criteria for the aerobot will follow as the fifth stage in the design. The sixth step in the process is to specify the localised values of the key parameters that are essential for the flight of the aerobot.

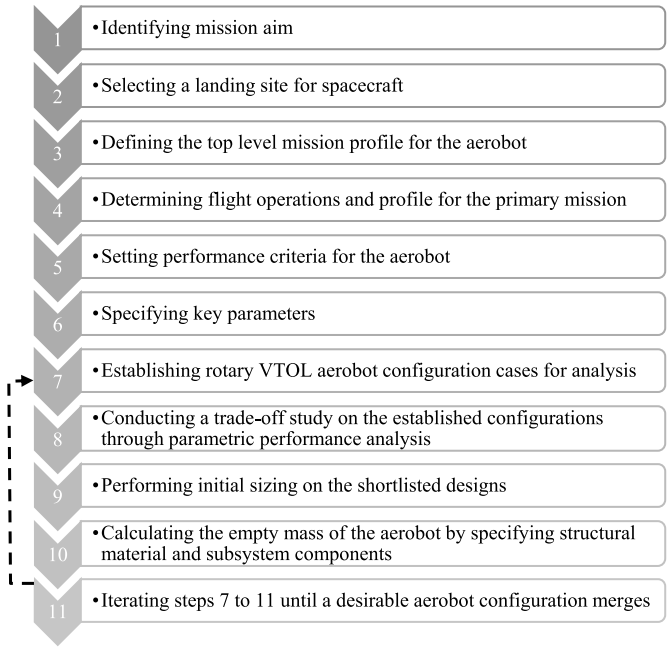

Fig. 1. Flow chart of the framework for the preliminary Martian aerobot design methodology.

The seventh step in the flow chart is to establish possible rotary VTOL aerobot configuration cases, along with specifying all the parametric values required for the performance analysis. The next stage is to perform the parametric performance analysis based on the methodology explained in section 5 for estimating the required flight power of rotorcraft configurations. In this eighth step, a trade-off study is conducted based on the results. The ninth step is to perform initial sizing on the shortlisted designs using the methodology explained in section 6 for the initial sizing, given it is a battery-electric aircraft. The second-last step is to calculate the empty mass (mass exclusive of payload and fuel) of the aerobot by identifying the components and materials of the structure of the whole system. Once the empty mass is determined, it will be utilised to balance the initial sizing equation. The outcome is unlikely to be desirable the first time and thus, it would require step 11 which is an iteration of steps 7 to 11 until an acceptable outcome is achieved. The subsequent sections provide detailed explanations and methods for each step using an example case, except for step 10, which is beyond the scope of this paper.

3. Mission statement and requirements

The first 5 steps of the framework for preliminary Martian aerobot design introduced in Fig. 1 are exemplified in this section by forming a mission scenario supported by relevant tools and methodologies. Starting with the identification of the mission aim and the justification of the selected landing site of the spacecraft, the top-level mission profile is defined using a mapping tool. Next, the flight operations and profile are determined based on the primary mission profile and current standard capabilities of an aerial drone in the Martian environment. Subsequently, the performance criteria of the potential Martian aerobot are framed by comparing its capabilities with those of recent mobile spacecraft operating on Mars' surface.

3.1. Mission aim identification

For over a decade, the Mars sample-return mission has remained a primary focus for NASA, ESA, CNSA, JAXA, Roscosmos, and other global space agencies. This mission not only enhances human understanding of Martian astrobiology but also lays the groundwork for future human exploration on Mars [22]. To mitigate mission risks and optimise scientific output, selecting a previously investigated region for the sample-return mission is imperative [23]. An aerial robot on the Martian surface, equipped with advanced scientific surveillance capabilities and significantly greater speed than a rover, stands as a crucial asset, accelerating the safe and efficient execution of the Mars sample collection mission. Therefore, the mission aim for this research project is to generate high-resolution aerial mapping of the area and mark potential experimental/sample collection points for future rover missions using a reusable VTOL aerobot.

3.2. Mission location requirement and justification

The design of the Martian aerobot must be adapted for the selected mission region. There can be numerous mission zones that can have one or more distinct territorial characteristics such as plains, highlands, arctic poles, underground caves, steep hills, and deep valleys. The selection of a landing site first requires fulfilling the criteria of engineering constraints and safe Entry, Descent, and Landing (EDL), as well as operation of the spacecraft. Post fulfilment of engineering constraints, the focus shifts to identifying scientifically significant sites. The Mars scientific objectives revolve around the major science goals; namely life, climate, geology, and preparation for human exploration, that are set by NASA's Mars Exploration Program Analysis Group (MEPAG) [24]. One of the ways to understand the selection of the landing site process is to look at the engineering parameters and requirements, particularly for sky crane-based EDL, alongside the science objectives of recent Mars missions such as the Mars 2020 mission (summarised in Table 1). Jezero Crater was selected from a database of 55 candidate landing sites for this mission because of its astrobiological importance while meeting engineering constraints.

The selected landing site on Mars for this study is the Southwestern (SW) Melas Basin within Valles Marineris which is the largest canyon system in the solar system (see Fig. 2a). Although ranked among the top 8 sites for previous NASA missions by planetary scientists [22], it was often rejected due to its rugged terrain and the extensive distances required to reach specific scientific locations [4]. However, now EDL in such terrain is possible because the Mars 2020 mission incorporated two new technologies, Range Trigger and Terrain Relative Navigation, for a precision landing in rougher terrain [25]. Accessing the designated Regions of Interest (ROIs) highlighted in Fig. 2b, such as delta and hydrated silica deposits, would require a rover drive of approximately 6 km, with travel times of less than 50 sols (Martian day) with a driving efficiency of 35–75 m/sol estimated in Ref. [22]. However, these evaluations were overly optimistic, as the actual driving efficiency observable from the Perseverance rover track record indicates values of <25 m/sol [26]. Thus, employing an aerial drone to map routes to ROIs aims to enhance rover driving efficiency, underscoring the necessity for a functional Martian aerobot equipped with scientific instruments in future.

3.3. Top-level mission profile definition

Valles Marineris extends over 4000 km, covering about one-fifth the circumference of Mars, with some parts running as deep as 7 km and as wide as 200 km [27]. Fig. 3 shows the mission operation profiles, including the estimated pathway of the aerobot and traverse distance calculated using JMars 5, a publicaly available geospatial information system (GIS) software [28]. The overall mission can be divided into three geographical sub-missions, marked with magenta, orange and yellow lines, that enable comprehensive coverage of the expansive canyon region systematically. This hierarchical approach aims to progressively boost confidence in the capabilities of the aerobot. Notably, other sections of the canyon, like East Melas Chasma, are among the 55 candidate landing sites [22]. The fundamental design of the aerobot is required to be based on the primary mission, which also includes the demonstration phase. Although, the longevity history of the spacecrafts that have landed successfully on Mars has shown that these do surpass expectations and carry on the scientific investigation for many years. Hence, the secondary and extended missions of an aerobot can be a good practice to be added to the list of design considerations. The definition of mission in terms of time and distance sets the foundation of the preliminary design and function of the aerobot. The primary mission of the aerobot would be to explore the SW Melas Basin, traversing a total of

Table 1
Summary of Mars 2020 mission landing site engineering constraints & safety criteria, and main scientific objectives [22].

Engineering Parameters	Landing Sites Requirements	Science Objectives			
Latitude	30°N to 30°S (due to surface thermal limitation)	Perform thorough in-situ science	*Geology:* Analyse the geological processes in a selected Martian area linked to ancient environments and diverse geology, indicating potential astrobiological importance.	Enabling the future	*Potential Sample Return:* Collect scientifically chosen samples with documented context, highlighting astrobiological importance and site geological diversity.
Elevation	<−0.5 km (Relative to datum)				
Landing Ellipse	≤16.0 km (West-East) 14 km (North-South)				
Rock Height	≤0.6 m				
Terrain Relief/Slopes	(length scale) 2–10 km: <20° 1–1000 m: ≤100 m relief				
Radar Reflectivity	Ka band reflective				
Load Bearing Surface	Not dominated by dust		*Astrobiology:* Evaluate the habitability of a historic Martian setting, examine materials conducive to preserving signs of life, and search for potential evidence of past life.		*Human Exploration/Technology:* Aid in preparing for Mars human exploration by addressing key knowledge gaps
Atmosphere	Up to 25 m/s horizontal and 20 m/s vertical winds during EDL				
Surface Winds for Thermal Environment for Rover Science Operations	During Operation: <15 m/s (steady) <30 m/s (gusts) Non-Operation (sleeping): <40 m/s (steady)				

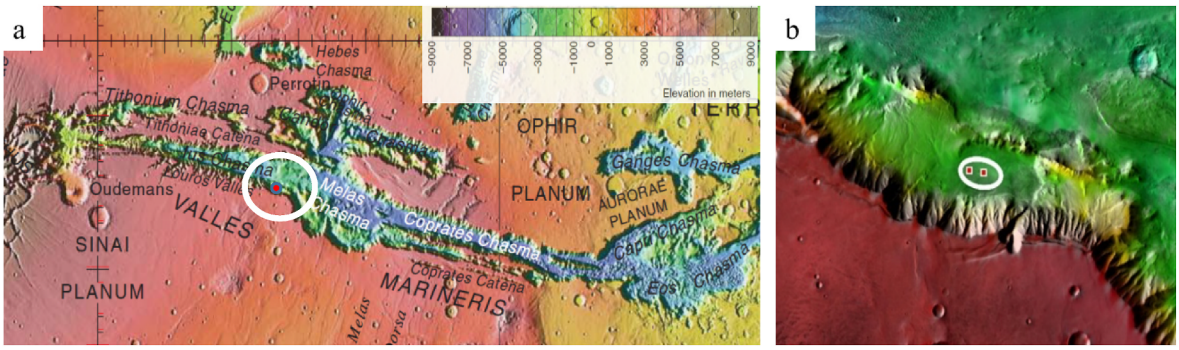

Fig. 2. a) Map showing SW Melas basin (red spot) in Valles Marineris. Cropped Topographic Map of Mars (M 25M RKN) by USGS 2003 based on data from the Mars Orbiter Laser Altimeter, an instrument on NASA's Mars Global Surveyor. b) Close-up of SW Melas Basin perches on the southwestern rim of Melas Chasma, with two ROI (red dots). The white outline (not to scale) is the 9.7 × 8.7 km landing ellipse centred at - 9.81° N, - 76.46° E, elevation −1.92 km [22]. Image created using JMars 5 (GIS) [28]. (For interpretation of the references to colour in this figure legend, the reader is referred to the Web version of this article.)

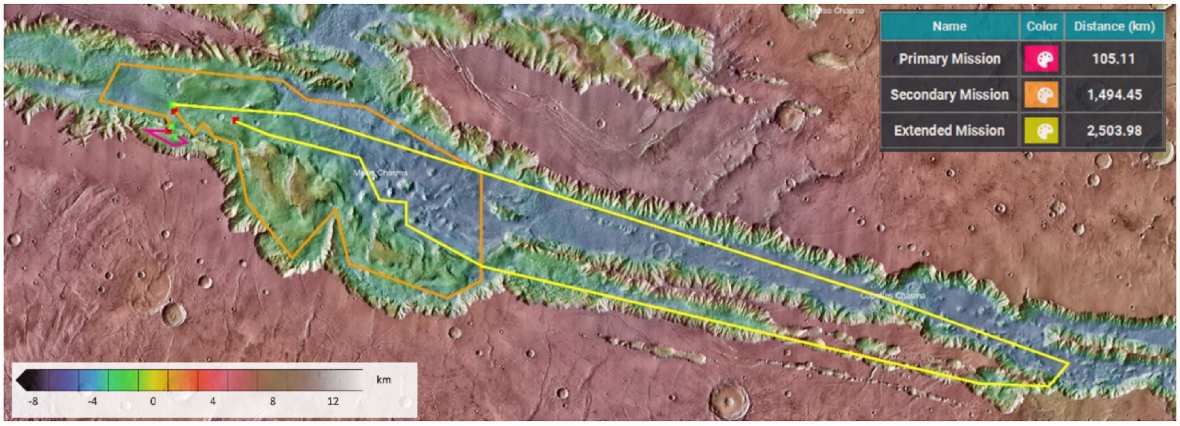

Fig. 3. Mission profile map showing Valles Marineris created in JMars5 (GIS) [28]. The green and red dots on each mission profile line depict the start and finish, respectively. (For interpretation of the references to colour in this figure legend, the reader is referred to the Web version of this article.)

~100 km, in the first ~30 sols after deployment. The secondary mission would explore the boundary of Melas Chasma, traversing a total of ~1500 km, in the next ~450 sols. The extended mission would explore the in-between of Melas Chasma and Coprates Chasma, traversing a total of ~2500 km, in the next ~750 sols. From this specified mission plan further specifications and parameters can be derived.

3.4. Flight operations and profile definition

Terrestrial mid-level electric battery-powered aerial drones commonly sustain an average flight time of ~20 min, while high-end consumer drones typically achieve ~30 min, with exceptions in some advanced drones and fixed-wing aircraft that can fly for several hours [29]. The flight duration on Mars is limited to short bursts due to the necessity of ensuring a sufficiently charged helicopter battery to avoid electrical issues during high-power manoeuvres. Effective energy management on Mars is important, with much energy allocated for temperature control, posing flight endurance challenges due to poor thermal dissipation in the thin Martian atmosphere [30]. The 20-min communication delay between Earth and Mars hinders real-time monitoring [31], relying on Earth station commands for aerobot navigation, limiting daily flights. Consequently, flight activities may occur intermittently, with much mission time devoted to tasks like charging, data transmission, and flight planning.

According to the primary mission objectives, the aerobot aims to traverse 100 km in 30 sols, translating to a total of 10 sols allocated for flight, with one sol dedicated to flying and two sols for data transmission and planning. This arrangement results in a range of 10 km per sol for

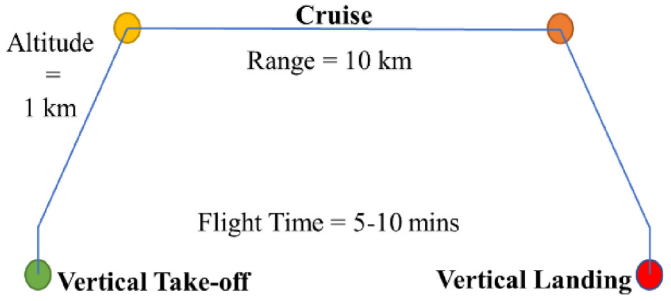

Fig. 4. Flight specifications and profile of an aerobot for the proposed Mars mission.

flight operations. Flight time range can be between 5 and 10 min, depending on the capability of the aircraft. A flight altitude of 1 km is selected, as aerial mapping at this altitude will ensure extensive coverage to bridge the gap between satellite and rover imaging. Fig. 4 summarises the selected specifications of the flight profile at which the aerobot would fly normally in pursuit of completing the missions defined above.

3.5. Aerobot's performance criteria establishment

A concise comparison between the Perseverance Rover, Ingenuity Helicopter, and the Potential Aerobot is presented in Table 2, outlining their mobility capabilities and mission-related requirements. The

Table 2
A comparison of requirements and capabilities between Perseverance Rover [26], Ingenuity Helicopter [2], and the Potential Aerobot (PA) according to the mission specification. Mars 2020 mission data is based on its completion of 1000 sols on Mars. 1 Martian year = 668 sols.

Metrics	Mars Spacecrafts			PA times (x) to	
	Perseverance Rover	Ingenuity Helicopter	Potential Aerobot (PA)	Rover	Ingenuity
Distance travelled per Martian year (km)	15	10	2227	149	222
Predefined Traverse Speed (m/s)[a]	0.04	2	22	556	11
Mean Operational Range per sol (km/sol)	0.022	0.015	3.33	149	222
Mean Number of Flights per Martian year (flights/yr)	NA	45	223	NA	5
Mean Operational Range per flight (km/flight)	NA	0.23	10	NA	44
Mean Operational Endurance per flight (min)	NA	1.5	7.5	NA	5

[a] Traverse speed of PA is based on the average flight time (i.e. 7.5 mins).

Potential Aerobot (PA) represents a hypothetical case study within the mission scenario, designed to evaluate the feasibility of long-range aerial exploration while offering comparative insights against existing ground systems on Mars. Notably, the Potential Aerobot demonstrates capabilities exceeding those of the Mars 2020 mission, which included both the Perseverance Rover and the Ingenuity Helicopter. Top-level performance requirements result from this comparison of a non-exhaustive list of metrics, which then inform the preliminary design of the aerobot. Compared to the rover, the Potential Aerobot can approximately cover 150 times more distance per Martian year and per sol on average, with about 550 times greater specified traverse speed, marking a significant advancement. When compared to the Ingenuity Helicopter, the Potential Aerobot's traverse speed is 11 times greater. However, it can be noticed that Ingenuity covered far less distance per Martian year than the rover. This inconsistency arose from the helicopter's lack of an independent communication system and its confinement to the vicinity of the Perseverance Rover, which restricted its mobility. Conversely, the Potential Aerobot is intended to possess higher traverse speed and fully equipped communication and navigation systems, enabling multiple long-range flights. As the design progresses, additional metrics for performance criteria will be necessary to delve into more specific design considerations.

4. Specification of key parameters

Specifying the parametric values that are central to the flight performance of the aerobot is the sixth step in the preliminary Martian aerobot design framework (Fig. 1). This section discusses methods and tools utilised to determine the values or a set of values of parameters such as air density, air viscosity, flight speed, rotor spin rate and rotorcraft size constraints. The key parameter upon which most of the aerodynamic calculations of the aircraft depends is the air density at which it will typically fly. The variation between air densities appears negligible, but a minute change can significantly impact the flying capability of rotorcraft in low-density environments like Mars. For instance, NASA's Ingenuity helicopter's thrust margin could drop from 30% to 8% with a slight decrease in air density from 0.0145 kg/m^3 to 0.012 kg/m^3 [34]. To compensate, the rotor speed must be maximised, leading to challenges such as encountering higher Mach numbers and addressing structural resonances. This highlights the sensitivity of rotorcraft operations to changes in air density, underscoring the requirement for precise measurements and adaptation of Martian rotorcraft designs to local atmospheric conditions for reliable performance. Overly optimistic values could falsely indicate superior performance in the aerobot design process, while overly conservative values may limit the demonstration of its full potential.

4.1. Approaches to local air density determination

Three approaches are presented to determine the air density on Mars for the design of the aerobot. The first approach provides the most generic estimate using the mean surface air density, which is 0.02 kg/m^3 on Mars [32]. This value reflects an overly optimistic atmospheric condition because regional air density depends on location and altitude from the datum (sea level), and varies across seasons and time of day. The second method for determining the air density involves a more specific approach based on NASA's Mars atmospheric mathematical model, which considers altitude effects and consists of separate equations for the lower atmosphere (<7 km) and the upper atmosphere (>7 km) [33]. In both zones, the temperature decreases linearly, and the pressure decreases exponentially with respect to the change in altitude. By inserting the desired altitude (H) value, measured above the ground, into Eq. (1) and Eq. (2), both temperature (T) and pressure (p) can be estimated, respectively. Different values of constants a and b are used in equations for the lower and upper atmosphere zones in Eq. (1) to determine temperature. Air density (ρ) is then calculated using Eq. (3) by inputting the corresponding values of temperature and pressure.

$$T_{\text{Celsius}} = -a - bH, \tag{1}$$

$$p = p_0 \mathrm{e}^{-H/H_0}, \tag{2}$$

$$\rho = \frac{p}{R(T_{\text{K}})}, \tag{3}$$

where T_{Celsius} ($^\circ C$) is the temperature on Celsius scale; H (m) is the altitude from the ground; p (kPa) is the atmospheric pressure; ρ (kg /m^3) is the air density; a ($^\circ C$) is a temperature intercept constant (=31 $^\circ C$ when H <7000 m; = 23.4 $^\circ C$ when H >7000 m); b ($^\circ C$ /m) is a lapse rate constant (=0.000998 $^\circ C$/m when H <7000 m, = 0.00222 $^\circ C$/m when H >7000 m); p_0(kPa) is a reference pressure constant (=0.699 kPa); H_0 (m) is an atmospheric scale height constant (=11111.1 m); R (kJ /kg /K) is a gas constant (=0.1921 kJ/kg/K); T_{K} (K) is the temperature on Kelvin scale (= T_{Celsius} + 273.15)

Continuing with the case study developed in the previous section 3, the Potential Aerobot requires flying from 0 to 1 km altitude according to the standard flight profile (Fig. 4). Applying this mathematical model at the surface (H = 0) and 1 km (H = 1000) altitudes yields an air density of 0.015 kg/m^3 and ~0.014 kg/m^3, respectively. These values are rather overly conservative estimates because although the model considers altitude effects, it does not account for atmospheric variations related to regional attributes such as datum level, seasons, and time of day.

The third technique for a more precise estimate of the local air density involves the utilisation of the Mars Climate Database (MCD Version 6.1) software [35]. This method requires additional knowledge about the red planet and inputs such as time of flight. Mars' calendar year has 12 months, which can be of varying numbers of sols depending on the solar longitude (Ls), which is a measure of the eccentric orbital position of Mars from the Sun. The span of 30° in Ls represents a month and the season on Mars changes after each 90° span, starting from the Northern Hemisphere's spring equinox (Ls = 0°) [35]. When applying this method to the Potential Aerobot mission scenario, the air density is estimated by taking the average of Mars regional air density spread across one Martian year with MCD's standard climatology scenario, for

the altitude of up to 1 km from the surface of SW Melas Basin. For a solar-powered autonomous aircraft, optimal flight times typically lean towards later in the day, allowing solar panels to recharge the battery after overnight heater use. However, a conservative local flight time of around 11 a.m. is used on Mars for regions in the middle latitudes, as delaying too long risks subjecting the rotorcraft to intensified winds due to increased solar heating in the lower atmosphere [30]. The MCD can present air density data output in two formats: a range presentation or distinct curves, as illustrated in Fig. 5. The graph in Fig. 5a depicts a visually coloured presentation of air densities over the range of 0–1000 m altitude at the 11th hour at SW Melas Chasma for a full Martian solar longitude range based on the climatology average solar scenarios. Conversely, Fig. 5b shows two distinct curves of air densities at 0 m and 1000 m altitudes under the same set of conditions.

The MCD is a publicly available reliable source, however, a discrepancy was found between these two graphs, as in Fig. 5b the maximum value of air density is about 0.0178 kg/m^3 (at 60° *Ls* and altitude 0 m), whereas in Fig. 5a it is 0.02 kg/m^3. Similarly, the minimum value of air density is about 0.0129 kg/m^3 (at 165° *Ls* and altitude of 1000 m) in the graph (b), as opposed to 0.014 kg/m^3 in the graph (a). Therefore, the average of the maxima and minima from both graphs is taken first, from which the mean value 0.016 kg/m^3 of the air density is determined that will be used in the initial aerobot sizing. Similarly, air viscosity data can be extracted from MCD. The viscosity estimates coinciding with the maxima and minima (at *Ls* of 60° and 165°, respectively) of air density are taken and then averaged. Hence, kinematic viscosity (=viscosity/density) is used to calculate the Reynolds number, which is required to define the accurate airfoil and streamlined aerodynamic body of the aerobot in the later stages of the design. For the secondary mission at East Melas Chasma (Latitude −12.22°N, Longitude 290.9°E), approximately 4 km below the datum, estimates for regional air density and air viscosity for various altitudes above the surface can be obtained using the same method. Air density reaches 0.025 kg/m^3 at the surface, indicating potential for improved flight performance during secondary missions.

4.2. Aerobot's size constraints definition

Another critical parameter is the geometric restriction imposed by the maximum allowable size of the aerobot. This constraint stems from the dimensions of the protective heat shield required for the Entry, Descent, and Landing (EDL) system, known as the aeroshell, which encases the spacecraft during transportation to Mars. Previous successful NASA EDL systems, such as the Pathfinder aeroshell (1997, 2.65 m diameter), Viking aeroshell (1976, 3.5 m), and Mars Science Laboratory (MSL) aeroshell (2012, 4.5 m), serve as benchmarks [5]. Fig. 6a shows the actual MSL aeroshell during testing, along with two Mars aerobot concept studies in the literature with folding mechanisms to fit into the Pathfinder aeroshell (Fig. 6b) and Mars 2020 mission aeroshell (Fig. 6c). The aeroshell size of the Mars 2020 mission was the same as that of MSL, which is currently the largest available aeroshell. Thus, this predefined limit sets the aerobot's maximum dimensions at 4.5 m in diameter and approximately 2.2 m in height. For the parametric performance analysis (step 8, Fig. 1) of potential design configurations in the Potential Aerobot case study, the rotor disk size range considered, excluding any rotor folding mechanism, spans from 5% to 100% (i.e., 0.23m–4.5m) of the aeroshell diameter.

4.3. Rotor speed limits determination

On Mars, where the speed of sound is approximately 240 m/s [4], operational constraints are imposed on rotor tip speed and forward velocity to mitigate the formation of transonic compression waves. In forward flight, the speed of the advancing blade is required to be approximately three times the airspeed of a helicopter to maintain lift on the retreating blade [36]. Typically, maximum rotor tip speed is constrained to be around 0.75 Mach (180 m/s). Therefore, a maximum forward velocity of 60 m/s is proposed, aligning with one-quarter of Mars' average speed of sound and conforming to one-third of the allowable maximum rotor tip speed. This means the RPM of the rotor must adjust so that the Mach number at the rotor advancing blade tip (M_{at}) does not exceed the maximum rotor tip speed during the forward flight. The term revolution per minute (*RPM*) is the rate at which the rotor spins and is calculated using the following equation:

$$RPM = \frac{60\omega}{2\pi} = \frac{60v}{2\pi r}, \tag{4}$$

where *RPM* (rev /min) is revolution per minute; ω (rad /s) is the angular velocity; v (m /s) is the rotor tip speed; r (m) is the rotor radius.

Smaller rotors require higher *RPM* than larger rotors to generate a similar amount of thrust. At the maximum permitted rotor tip speed (i.e., 180 m/s), the *RPM* ranges from approximately 15000 for a 0.23 m rotor to 800 for a 4.5 m rotor. Ingenuity, with a 1.2 m rotor disk, had a maximum allowable *RPM* of ~2800 [30].

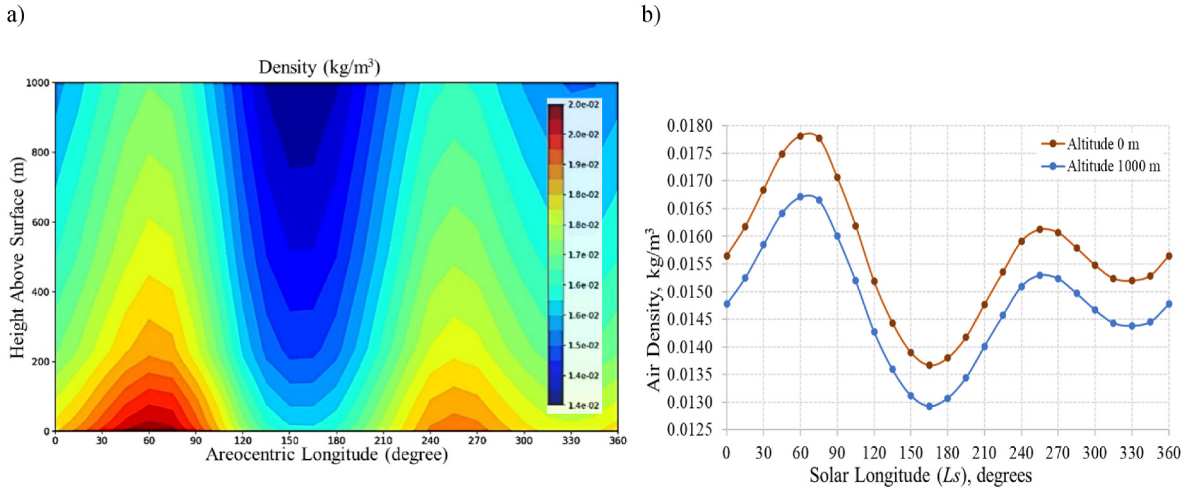

Fig. 5. The graphs show air density over the altitude above the local surface of SW Melas Chasma (Latitude −9.81N. Longitude 283.5E.) at a local time of 11.0 h, spread over the full range of Martian Solar Longitude. a) altitude range of 0 m–1000 m. b) at altitude 0 m and 1000 m. MCD_v6.1 with climatology average solar scenario [35].

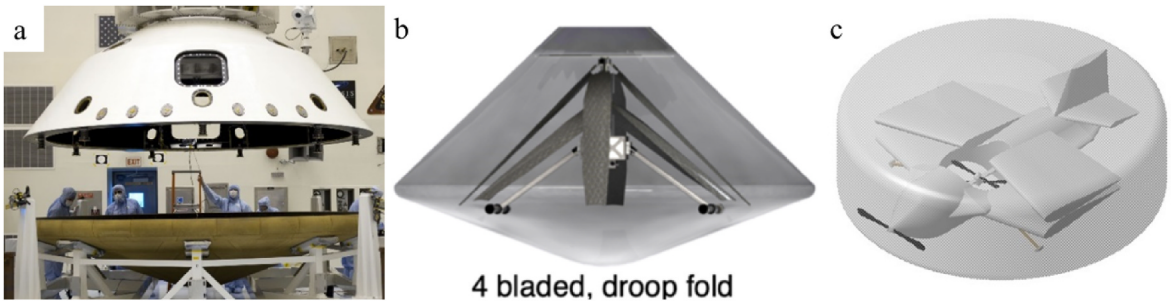

Fig. 6. a) Mars Science Laboratory aeroshell during testing (2011, size 4.5 m). Credits: NASA/Kim Shiflett. b) Folding option for coaxial helicopter concept in Pathfinder Aeroshell (size 2.65 m) [5]. c) Winged VTOL concept CAD model called FuMAD, folded and packed in Mars 2020 mission aeroshell (size 4.5) [37].

5. Methodology for estimating required flight power of rotorcraft configurations

The section introduces a generalised methodology derived to estimate the power requirements of various rotorcraft configurations for the conceptual design of a next-generation Martian drone. This estimation is important for the trade-off analysis (step 8 of the design framework illustrated in Fig. 1), later applied in sections 8 and 9 to select an appropriate configuration for the Potential Aerobot (the hypothetical case study) on Mars. The analysis uses conservative values for most of the coefficient-type variables. Fig. 7 depicts possible configurations with single and dual rotors, extensively utilised as VTOL aircraft for terrestrial applications. A standard/conventional helicopter is equipped with a single main rotor situated on top and a tail rotor positioned at the rear. While the main rotor provides lift and propulsion, the tail rotor counteracts the torque generated by the rotation of the main rotor. Conversely, a coaxial helicopter features two rotors aligned on the same axis, rotating in opposite directions, eliminating the need for a tail rotor. This design enhances stability and manoeuvrability. Tandem rotorcraft have dual main rotors, one placed in front of the other on the same body. This configuration offers substantial lift capacity and efficient load-carrying capabilities. Side-by-side rotorcraft have multiple rotors positioned next to each other, typically on the same horizontal plane. This category includes versatile configurations like tiltrotors and tiltwings, allowing for both hovering and forward flight. Quadcopters and hexacopters, types of multicopter, feature four and six rotors, respectively, and are well-known for their simplicity, stability, redundancy, and ease of control. This paper focuses on estimating the power requirements and comparing configurations, including conventional rotorcraft, coaxial rotorcraft and tandem rotorcraft.

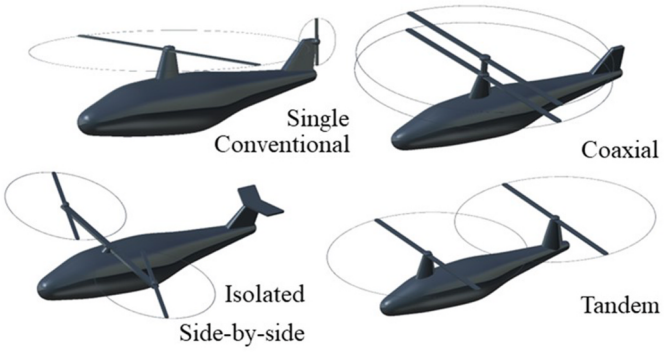

Fig. 7. Illustration of existing rotorcraft configurations: Single Conventional, Coaxial, Tandem and Isolated Side-by-side rotors.

5.1. Single rotor conventional rotorcraft

For a reusable Martian aerobot to achieve successful flight, its ability to execute vertical takeoff and landing (VTOL) is critical, as runways are unavailable on Mars. This capability hinges entirely on the rotary propulsion system of the rotorcraft. Momentum theory is utilised to estimate the power (P) consumption of the rotor during hover, vertical climb, and forward flight. This theory assumes that spinning rotor blades act as an actuator disk with minimal thickness and a specific disk area (S). The model also assumes a uniform airflow across the rotor disk and instantaneous energy transfer to the airflow. Additionally, factors like airfoil profile drag losses, tip losses, and residual rotational velocities are disregarded. To adjust for these losses, a parameter called the figure of merit (M) is introduced. This figure ($M = P_{\text{ideal}}/P_{\text{actual}}$) represents the ratio of ideal power to actual power and serves as an indicator of rotor efficiency. The equation provides the necessary power for vertical (vert) climb or hover (when the climb velocity is zero), specifically formed for a conventional helicopter [36].

$$P_{(\text{Vert Climb or Hover})} = \left[\left(\frac{fW}{M}\sqrt{\frac{fW/S}{2\rho}}\right)+\frac{WV_{\text{Climb}}}{2}\right]\left[\frac{(1+P_{\text{tail rotor}}/P_{\text{main rotor}})}{\eta_{\text{mechanical}}}\right], \tag{5}$$

where P (Watt) is the power required; W (N) is the rotorcraft weight ($=mg$, where m (kg) is the mass of the rotorcraft and g (m/s^2) is the surface gravity acceleration on Mars for the sake of this paper); S (m) is the rotor disk area; M is the figure of merit; V_{Climb} (m/s) is vertical climb velocity ($=0$ for hover); f is the adjustment for downwash on the fuselage ($=1.06$ typically); ρ (kg/m^3) is the local air density on Mars; $\eta_{\text{mechanical}}$ is mechanical losses adjustment due to driving of the tail rotor ($=0.97$ typically).

The calculated total power encompasses the power requirement for the tail rotor as well. Generally, the ratio of power needed by the tail rotor to that required by the main rotor ($P_{\text{tail rotor}}/P_{\text{main rotor}}$) ranges between 0.14 and 0.22, as tail rotors usually have a diameter of approximately 15–20% of the main rotor's diameter [36].

During forward flight, the rotor functions similarly to a circular wing. The aspect ratio of such a wing stands at $4/\pi$, featuring an equivalent Oswald efficiency factor between 0.5 and 0.8, based on empirical observations [36]. The Oswald efficiency factor defines the efficiency of the wing concerning induced drag and is calculated as the ratio between the wing's induced drag coefficient to that of an equal aspect ratio elliptic wing at the same lift coefficient. Parasitic drag can be quantified using the drag area (D/q), where 'q' denotes the dynamic

pressure. The following equation integrates these elements to generate required power approximations for forward climb or level flights [36].

$$P_{(\mathrm{Fwd_{climb}\ or\ Fwd_{level}})} = \left[\frac{V}{\eta_p}\left\{q(D/q)+\frac{W^2}{4eqS}+W\sin(\gamma)\right\}\right]\left[\frac{(1+P_{\mathrm{tail\ rotor}}/P_{\mathrm{main\ rotor}})}{\eta_{\mathrm{mechanical}}}\right], \quad (6)$$

where V (m/s) is the forward flight speed; γ (Deg) is the climb path angle (=0, when levelled); q (Pa) is the dynamic pressure; e is the equivalent Oswald's efficiency factor (=0.5 to 0.8 typically); D/q (m^2) is the component drag area; η_p is the propeller efficiency (=0.6 to 0.85 typically).

In this equation, $W\sin(\gamma)$ represents the climb component, contingent upon the climb path angle γ (which is 0 for level flight). The rotor, while generating lift, also serves as a propeller for forward propulsion. Hence, to provide a reasonable estimate of the rotor in forward thrust, the propeller efficiency factor η_p is incorporated into the calculation.

5.2. Coaxial rotorcraft

In a traditional helicopter setup, the primary function of the tail rotor is to counteract the torque produced by the rotation of the main rotor. It is achieved by generating an opposing thrust force, effectively balancing the torque. An alternative solution is to use another similarly sized rotor that spins in the opposite direction. This secondary rotor generates thrust parallel to the main rotor, offering the added benefit of increased lift. This concept is employed in the coaxial rotorcraft configuration, where two rotors are situated on the same shaft within a more complex hub arrangement. This configuration may suggest a doubling of the lift force; however, the close proximity of the rotors results in the loss of some lift due to airflow wake interference. Theoretically, when the two rotors entirely overlap, known as a 100% overlapping case with zero vertical separation, the overlapping interference factor (K_{ov}) raises power consumption by $\sqrt{2}$, or approximately 41%, compared to two isolated rotors that are unaffected by the upper rotor's wake [38]. When the rotors are aligned without any vertical spacing in a coaxial setting, it is termed an equivalent single rotor. This equivalent single rotor equates to a system of smaller paired rotors with identical total thrust and total projected area (disk loading). This equivalence is due to their shared rotor solidity, defined as the ratio of total blade area to total disk area [39].

In practical applications, coaxial rotor systems maintain a physical separation between the two rotors. With increased vertical separation, the wake of the upper rotor affects a smaller area of the lower rotor, leading to a reduction in the overlapping interference factor (K_{ov}). For instance, with large separation (indicated as LS in section 8), typically around 10% of the rotor diameter, the K_{ov} decreases to 1.281 under the assumption of uniform disk loading [38,39]. Hence, to calculate vertical climb and hover power for a coaxial rotor system with equally sized rotors sharing the total rotorcraft weight, Eq. (5) is adjusted by multiplying it by the overlapping interference factor (K_{ov}), resulting in Eq. (7). Similarly, Eq. (6) for a forward flight of a traditional helicopter is adapted to form Eq. (8) for a coaxial helicopter [38].

$$P_{(\mathrm{Vert\ Climb\ or\ Hover})} = \left[\left(\frac{fW}{(2\sqrt{2})M}\sqrt{\frac{fW/S}{2\rho}}\right)+\frac{WV_{\mathrm{Climb}}}{4}\right]\left[\frac{2}{\eta_{\mathrm{mechanical}}}\right][K_{ov}] \quad (7)$$

$$P_{(\mathrm{Fwd_{climb}\ or\ Fwd_{level}})} = \left[\frac{V}{\eta_p}\left\{q(D/q)+\frac{W^2}{16eqS}+\frac{W\sin(\gamma)}{2}\right\}\right]\left[\frac{2}{\eta_{\mathrm{mechanical}}}\right][K_{ov}] \quad (8)$$

In this configuration, there is no tail rotor; instead, a second rotor is utilised. Consequently, the ratio of power required by the two equal-sized rotors ($P_{\mathrm{second\ rotor}}/P_{\mathrm{main\ rotor}}$) becomes 1.

5.3. Isolated rotors (non-overlapping rotors e.g., rotorcrafts with side-by-side rotors)

The K_{ov} factor, signifying the degree of overlapping interference between two identically sized rotors, changes from $\sqrt{2}$ to 1 when the shared area between them in the same plane shifts from full to zero. In the latter case, these rotors essentially function as isolated entities. Although there might be a minor degree of either beneficial or detrimental interference when there is a vertical separation between the rotors without any overlap, this aspect is usually disregarded in preliminary studies [38,39]. For example, one subtype of side-by-side rotors is transverse rotorcraft, including tiltrotors and tiltwings, where smaller rotors are mounted horizontally on the tips of side wings or an extended support frame of the fuselage. Typically, these smaller rotors are positioned to avoid overlap and function similarly to isolated rotors. During the cruise flight, they transition into forward propellers. In scenarios involving configurations with multiple non-overlapping rotors, Equations (5) and (6) can be modified to accommodate a multirotor system with an 'N' number of equally sized rotors. In such an arrangement, the total thrust required for the rotorcraft is assumed to be evenly distributed among all the rotors, as described in Equations (9) and (10).

$$P_{(\mathrm{Vert\ Climb\ or\ Hover})} = \left[\left(\frac{fW}{(N\sqrt{N})M}\sqrt{\frac{fW/S}{2\rho}}\right)+\frac{WV_{\mathrm{Climb}}}{2N}\right]\left[\frac{N}{\eta_{\mathrm{mechanical}}}\right] \quad (9)$$

$$P_{(\mathrm{Fwd_{climb}\ or\ Fwd_{level}})} = \left[\frac{V}{\eta_p}\left\{q(D/q)+\frac{W^2}{(N^2)4eqS}+\frac{W\sin(\gamma)}{N}\right\}\right]\left[\frac{N}{\eta_{\mathrm{mechanical}}}\right] \quad (10)$$

However, in forward flight setups where the rotors align in front of each other, there is an additional downwash effect generated by the front rotor onto the rear rotor. To estimate the actual power required, this downwash must be considered and factored into the rear rotor/s [38], as explained in subsection 5.4 about the tandem rotorcraft. As there is no tail rotor in this configuration, but all equally sized rotors, thus the segment $[1+(P_{\mathrm{tail\ rotor}}/P_{\mathrm{main\ rotor}})]$ of the original equation is replaced by $[N]$ in the modified equation to reflect the number of rotors involved.

5.4. Rotorcraft with partial overlapping rotors (e.g., tandem rotorcraft)

The longitudinal configuration of a tandem rotorcraft involves aligning two equal-sized rotors along the fuselage, with one rotor situated in front of the other. The theoretical analysis of this setup resembles that of coaxial rotors as it generally includes a certain degree of overlapping disk area, determined by the horizontal gap between the rotors. Maximum tandem overlap occurs when one rotor's blade tip touches the hub centre of the other rotor. Therefore, the initial assessment for vertical climb or hover power in tandem rotors employs the same equation Eq. (7) as used for coaxial rotors. However, the determination of the overlapping interference factor (K_{ov}) in a tandem configuration is influenced by the ratio (d/D), representing the horizontal distance (d) between the two rotor axes and the rotor diameter (D), as illustrated in the tandem rotor configuration top view in Fig. 8. When the rotors are in the same plane (i.e., no vertical gap between rotors), demonstrated in Fig. 8 side view (a), K_{ov} can be approximated using Eq. (11) [38]. In scenarios where rotors operate in separate planes (side view (b), Fig. 8), and the lower rotor functions within the contracting wake of the upper rotor, determining the overlapping area necessitates numerical integration to ascertain a solution for K_{ov}.

$$K_{ov} = \left[\sqrt{2}-\frac{\sqrt{2}}{2}\left(\frac{d}{D}\right)+\left(1-\frac{\sqrt{2}}{2}\right)\left(\frac{d}{D}\right)^2\right] \quad (11)$$

In forward flight estimation for tandem rotorcraft, the downwash from the front rotor affects the rear rotor, which requires calculation and

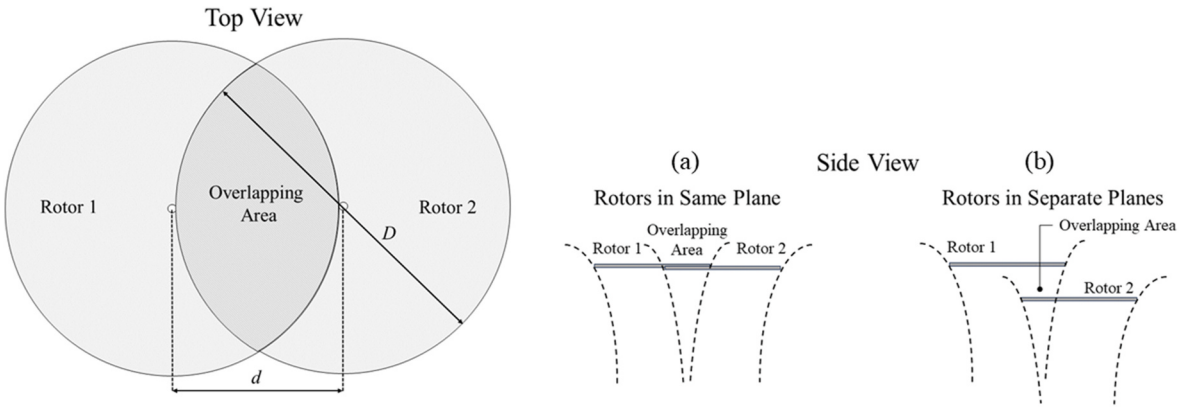

Fig. 8. Schematic illustration of tandem rotors overlapping area showing a generic top view and side view of rotors in the (a) same plane and (b) separate planes. (Not to scale).

must be added to the power loss. For preliminary theoretical analysis, this downwash (dw) is presumed to reach the maximum value of the overlapping interference factor (max $K_{ov} = K_{dw}$) [38], calculated as 1.134 with maximum tandem overlap using Eq. (11). Therefore, the total power (P) required for forward flight is described in Eq. (12) [38]. For initial assessments, it is assumed that the two equally sized rotors generate identical thrust and thus, necessitate equal power. Hence, this expression is formulated in Eq. (13), where the total power of two isolated rotors is halved, and then one-half is multiplied by the downwash factor.

$$P_{(\text{Forward})} = P_{\text{Front Rotor}} + P_{\text{Rear Rotor}}(K_{dw}), \tag{12}$$

$$P_{(\text{Forward})} = (1 + K_{dw})\frac{1}{2}P_{2\ \text{Iso}}K_{ov}\ , \tag{13}$$

where $P_{2\ \text{Iso}}$ (Watt) is the required forward flight power of rotorcraft with 2 isolated rotors; K_{dw} is the downwash factor (=1.134); K_{ov} is the overlapping interference factor (=1, when no overlapping).

When there is an overlap between the rotors, equations (7) and (13) incorporate the parameter K_{ov}, which is calculated using Eq. (11), to estimatehover, vertical climb and forward power, respectively. However, in scenarios where there is no overlap between the rotors, such as in non-overlapping same-plane tandem rotors, the K_{ov} factor is either omitted or the value is set to 1 in equations (7) and (13). This adjustment is necessary because using Eq. (11) for K_{ov} estimation is invalid when there is no overlap between the rotors.

Additionally, side-by-side rotor configurations with overlapping rotors can utilise a comparable approach to evaluate the overall power required. One such configuration is the synchropter, characterised by two counter-rotating rotors set at outward-tilting angles and a single gearbox to prevent blade collisions. This configuration would require numerical integration, and, for this reason, it is not considered a viable configuration for this study. Each of these rotorcraft configurations possesses distinct characteristics and aerodynamic considerations, and the selection among them is based on specific mission requirements and design objectives [38,39].

6. Methodology for the initial sizing of battery-electric aerobot

In this section, methodologies are outlined for estimating battery mass based on flight power requirements and conducting initial sizing for aerobot mass estimation, essential for step 9 of the design framework (Fig. 1). These methods are applied in section 9 using the ongoing example study case to determine the Potential Aerobot's empty mass. The total mass of an aircraft at maximum take-off comprises three primary elements: the empty mass, the payload, and the fuel. In the case of conventional fuel-powered aircraft, mass decreases progressively during flight due to fuel consumption across multiple flight phases, including taxiing, take-off, ascent, cruising, and descent. This decrease in mass affects the performance of aircraft and aerodynamic properties, necessitating detailed calculations for each flight phase during initial sizing estimations. However, in the case of electric aircraft, there is no variation in battery mass during flight. Consequently, there is no need for integration across different flight segments. Instead of fuel, the total mass of the aircraft includes the mass of the battery (m_b). The necessary battery mass for the flight mission is determined through the Battery Mass Fraction (*BMF*), represented in Eq. (14) as the ratio of battery mass to the total aircraft mass (m_b/m_0) [36].

$$BMF = \frac{m_b}{m_0} = \frac{W_b}{W_0} = \frac{EP_{\text{used}}}{E_{sb}\eta_{b2s}m_0}, \tag{14}$$

where m_0 (kg) is the total take-off mass of the aerobot; m_b (kg) is the battery mass; W_0 (N) is the total take-off weight of the aerobot (=mg, where g (m/s^2) is the surface gravity acceleration on Mars for this paper); W_b (N) is the battery weight; P_{used} (Watt or W) is the power required; E (hour or h) is the known run time; E_{sb} (Wh/kg) is the battery-specific energy; η_{b2s} is the total system efficiency from the battery to the motor output shaft (=0.9 typically).

Equation (14) accounts for parameters such as the known endurance (E) and power consumption (P_{used}) during distinct flight segments, including vertical climb, hover, and forward flight for rotorcraft. To obtain the total required aircraft *BMF*, the *BMF*s for each flight segment are summed. This method enables a comprehensive evaluation of the battery mass required for different phases of the mission flight profile of the aerobot [36].

When calculating the Battery Mass Fraction for electric aircraft, it is important to later include nominal usage and discharge efficiency to improve the precision of battery mass estimations. Nominal usage refers to the usable portion of the battery's capacity, as batteries are typically not discharged from 0% to 100% to prevent degradation and extend lifespan. For instance, operating within a range of 10%–80% state of charge limits useable capacity to 70%, reducing stress and enhancing longevity [40]. Discharge efficiency, defined as the ratio of energy output during discharge to energy input during charging, also influences battery sizing. A discharge efficiency of 95%, for example, indicates that 5% of the energy is lost, primarily as heat [41]. Incorporating these adjustments into the *BMF* ensures the aircraft achieves its performance objectives while safeguarding battery health and operational reliability.

The total aircraft take-off mass is determined by the sum of the empty mass (m_e), battery mass, and payload mass, as shown:

$$m_0 = m_e + m_b + m_{\text{payload}} \tag{15}$$

To adjust this equation for battery-electric aerobot sizing, Ref. [36] applied a modification to derive the following equation:

$$m_0 = \frac{m_{payload}}{1 - BMF_{total} - \frac{m_e}{m_0}} \quad (16)$$

This adaptation involves considering the total Battery Mass Fraction and the ratio between the empty mass and the total take-off mass [36]. Within this framework, the payload can encompass instrumentation or delivery items, especially in the context of unmanned aircraft. Conversely, the term m_e comprises all the components apart from the payload or operational batteries. This includes the propulsion system, aircraft structure, avionics, navigation systems, and other critical components necessary for the functionality of the aerobot, along with a percentage contingency margin.

The initial sizing equation serves as a foundational reference, allowing for preliminary measurements based on factors like the empty mass ratio, payload mass (derived from statistical data or a particular package), and the calculated Battery Mass Fraction (*BMF*). This equation provides a starting point to determine the total take-off mass of the aerobot. Alternatively, known or predetermined parameters can be used to estimate unknown variables; for instance, the empty mass, when total take-off mass and payload are known, and the required battery mass is computed using calculated *BMF*. This iterative procedure permits multiple calculations and adjustments until a reasonably accurate estimate aligns with the desired objectives, thereby facilitating comprehensive preliminary design investigations.

7. Establishing rotorcraft configuration cases for parametric analysis

As per step 7 of the framework for the preliminary Martian aerobot design (Fig. 1), this segment establishes the potential rotorcraft configuration cases and sets values for all parameters, and a range for variables, in alignment with mission requirements for parametric performance analysis for the example mission scenario developed in the earlier sections. For rotorcraft with multiple equal-sized rotors, some generalisations can be made. When the rotor diameter (D) equals or falls below the half value of the maximum allowable diameter (D_{max}) – the disk size beyond which the blade would hit the hub of the other rotor – the rotors do not overlap and are deemed isolated. Where the rotor size is above half D_{max}, the rotors overlap and behave as an overlapping tandem rotor setup, as expressed by the following equation:

$$D_{non-overlap} \leq \frac{D_{max}}{2} < D_{overlap} \quad (17)$$

The above relationship is expressed in Fig. 9 along with the rotor hub position (h), which represents the displacement from the reference point/line located in the middle of two adjacent rotors (i.e., the reference line shown); which when factored by 4 gives D_{max} as shown in Eq. (18) and when factored by 2 it estimates the horizontal distance (d) between the two rotor hubs, Eq. (19).

$$D_{max} = 4h = 2d, \quad (18)$$

$$d = 2h, \quad (19)$$

where D_{max} (m) is the maximum allowable rotor diameter; h (m) is a displacement from the reference point/line located in the middle of two adjacent rotors; d (m) is the horizontal distance between the two rotor hubs.

For the given aeroshell dome size limit (A), the rotor hub position at which the maximum allowable rotor diameter is within the aeroshell without requiring any folding mechanism can be deduced by the following equation, which is valid for the rotors in tandem settings (e.g. Fig. 11, Case 3).

$$h = \frac{A}{6} \quad (20)$$

7.1. Tandem rotorcraft configuration cases formation

Tandem rotorcraft configurations can vary based on the longitudinal positioning of the rotors atop the fuselage. For power analysis, three cases are examined based on the structural limits of the aeroshell, assuming the fuselage matches the maximum aeroshell size of 4.5 m. The hubs of two equal-sized rotors are positioned at equal distances from the middle of the fuselage at 2.25 m, 1.125 m, and 0.75 m for Cases 1, 2, and 3, respectively as shown in Fig. 10. These positions represent extreme scenarios for parametric analysis, with Case 1 placing foldable rotors at the end of the fuselage with a maximum allowable diameter of 9 m, while Case 3 positions rotors to reach a maximum permitted diameter of 3 m that fits within the aeroshell boundary, and Case 2 setting falls between these two cases, which allows rotors to a maximum diameter of 4.5 m (Fig. 11). A summary of the defined parameters for all three tandem rotorcraft configuration cases is detailed in Table 3. Tandem Case 1 requires a folding mechanism and possibly an articulated rotor hub system for storage within the aeroshell. Similarly, Case 2 would demand folding mechanisms and perhaps an articulated rotor hub system as well, if the rotor diameter exceeds 2.25 m. Contrary to

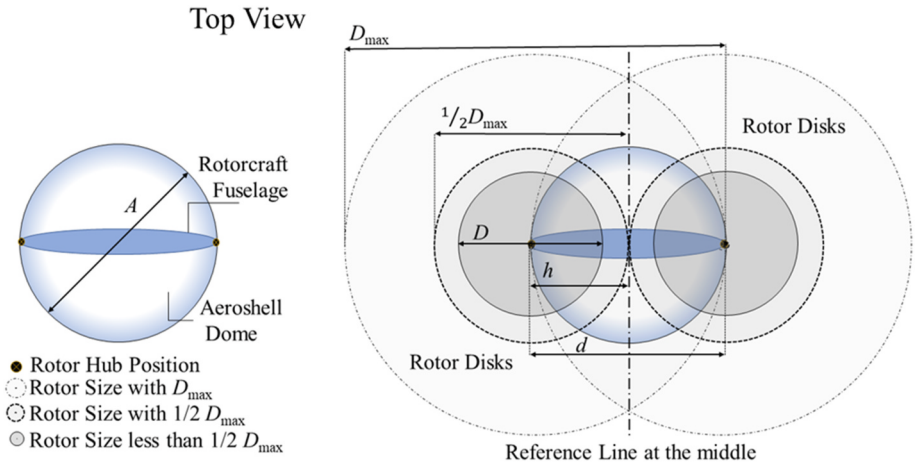

Fig. 9. Schematic diagram illustrating the terms A, D_{max}, h, d. Left side image shows a fuselage of the rotorcraft within a spacecraft aeroshell highlighting the size limit A. Right side image shows 3 different sizes of rotor disks at a fixed rotor hub position, demonstrating how changes in rotor diameter affect the degree of rotor overlap.

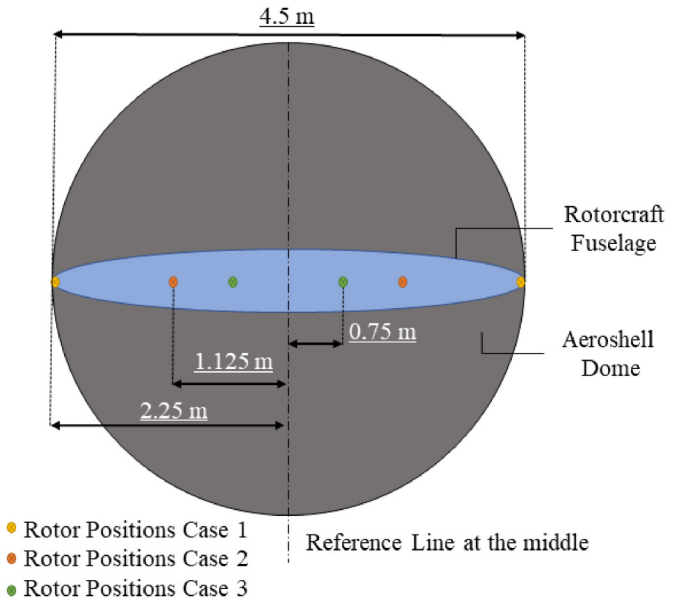

Fig. 10. Schematic illustration of three cases of tandem rotor hub positions on the fuselage placed inside the aeroshell. (Not to scale).

this, Case 3 can utilise a rigid rotor hub system without requiring linkages. Notably, the practical design considerations, such as the clearance between rotor blades and aeroshell walls or rotor hubs, have not been factored into this theoretical analysis.

7.2. Parameters and variables finalisation

The initial sizing of the rotorcraft incorporates the total flight mission duration based on range, cruise speed, takeoff, and climb, presuming continuous high-power operation, initially excluding descent and landing times to simplify analysis [36]. Therefore, the flight profile considered in this analysis, Fig. 12, involves a 2-min ascent to 1 km (resulting in an average vertical climb velocity (V_{climb}) of 8.33 m/s) and a 3-min traverse of 10 km (yielding an average cruise velocity of 55.56 m/s) and vertical descent, totalling 5 min.

For the Potential Aerobot case study, the Maximum Take-Off Gross (MTOG) mass of the aerobot for the mission is set to be 20 kg. The figure of merit (M), typically ranges between 0.6 and 0.8 for a full-scale helicopter on Earth [36]; however, because of the low Reynolds number on Mars the lowest value of 0.6 is used for this analysis as a conservative choice. The battery specific energy (E_{sb}) required for Battery Mass Fraction (BMF) calculations for flight is selected to be 230 Wh/kg pack (including battery management system), sourced from a JPL technology forecast [5]. Concerning forward flight analysis, certain parameters are crucial, such as the frontal area of the aircraft body. For all configurations, the same frontal area comprising the fuselage, landing legs, and an unfaired rotor hub is considered. Helicopter-specific drag data, outlined by D. Raymer [36] in terms of drag area (D/q) per unit frontal area, is used. This drag area data, when multiplied by the frontal area of the helicopter, provides specific values for the drag area of each component. The calculated total parasitic drag is subsequently integrated into the forward flight power Eq. (6) for conventional helicopters, and similarly included in the respective forward flight equations for other rotorcraft configurations. While this drag data method is not precise, it is sufficient for the initial sizing of the rotorcraft until the design matures for a comprehensive preliminary study. The theoretical method used aligns well with experimental data in the literature, particularly within an advance ratio range of 0.1–0.3 [38]. The advance ratio of rotorcraft is the ratio of its forward flight speed to its rotor tip speed. Table 4 summarises the parameters and variables defined for this research used in the parametric power analysis for various rotorcraft configurations during forward flight, vertical climb, and hover phases.

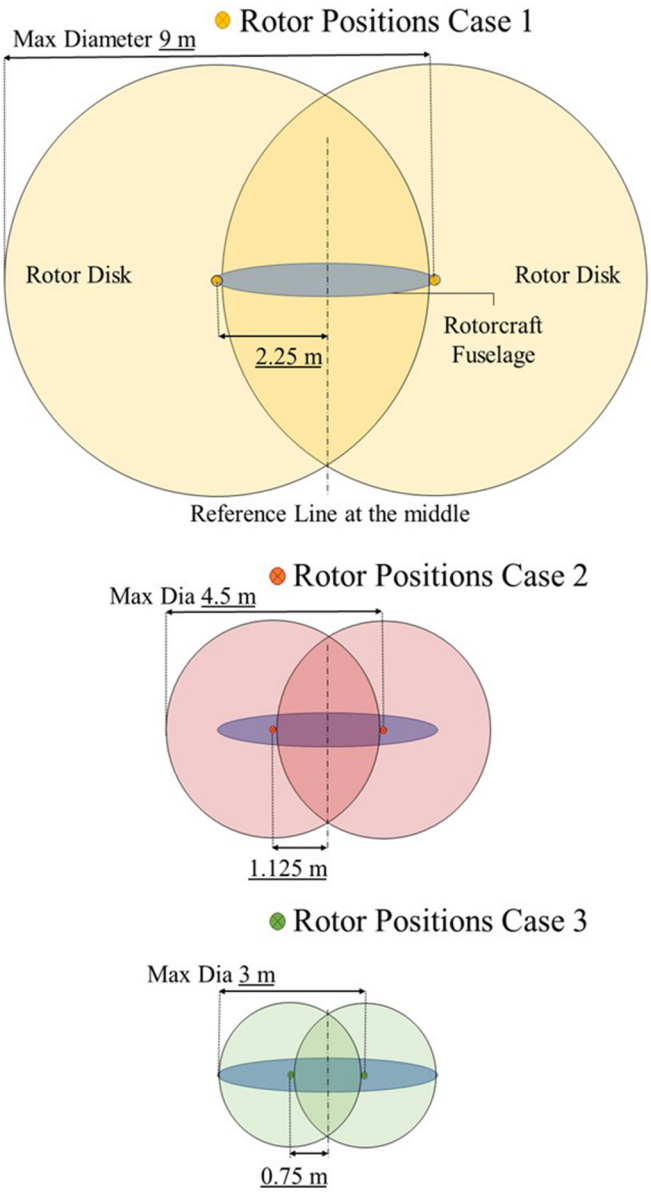

Fig. 11. Schematic illustration of the rotor positioning of tandem rotorcraft cases 1, 2 and 3 in operational mode. (Not to scale).

Table 3
Summary of tandem rotorcraft cases

Case No.	Rotor System Type	Folding Mechanism	Maximum Diameter	Rotor Position[a]	Isolated Rotor behaviour
1	Articulated	Yes	9 m	2.25 m	$D \leq 4.5$ m
2	Articulated[b]	Yes[b]	4.5 m	1.125 m	$D \leq 2.25$ m
3	Rigid	No	3 m	0.75 m	$D \leq 1.5$ m

[a] Rotor hub position from the center of the fuselage.
[b] When rotor D is $>$ 2.25 m.

8. Results and analysis

Continuing within the framework for preliminary drone design for Mars (Fig. 1), the following stage (step 8) involves the evaluation and

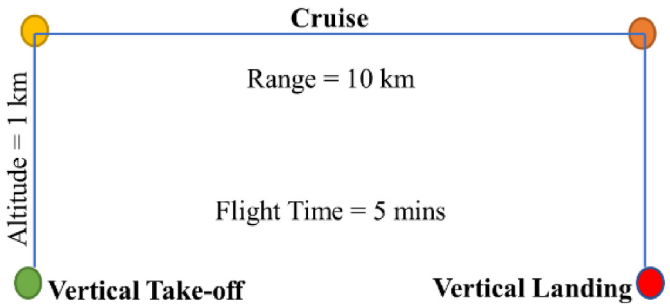

Fig. 12. Flight profile for the analysis.

selection of various rotorcraft configurations based on their power consumption within a simplified flight envelope. This trade-off study, conducted through parametric performance analysis, utilises the methodology outlined in Section 5 to assess different configurations and parameters introduced in the previous section (7). The objective of the parametric analysis is to identify the most suitable configuration for the exemplar mission outlined in Section 3, although the same approach can be applied to any other VTOL aerobot mission on Mars. The subsequent subsections present results and analysis in terms of power requirements for hover, vertical climb, and forward flight segments for rotorcraft configurations with single and dual rotors, including a single conventional, coaxial rotors with large separation (LS), three cases of tandem rotors (shown in Fig. 11) and 2 isolated rotors. These findings inform the sizing of battery packs and, consequently, the overall mass of the rotorcraft. Later, Section 9 will present a further discussion of the results and the practical implications of the analyses.

8.1. Hover and vertical climb analysis

Fig. 13 shows the power demand for a Martian helicopter of conventional configuration plotted against the increasing diameter of the rotor disk. As the rotor size expands, the area of the rotor disk also increases, leading to a reduction in disk loading. Disk loading is the ratio of the total weight of the helicopter to the area of the rotor disk (W/S). This means that by using motor power on a larger air cross-section, the helicopter achieves greater thrust efficiency. Consequently, when disk loading decreases, there is a reduced requirement for battery and motor power during hovering or climbing. This reduction in power demand allows for a higher power loading (W/P), which represents the ratio of the helicopter's weight to its engine power. However, it is important to note that while lower disk loading, associated with larger rotor blades, can improve efficiency, it can also lead to increased weight, higher forward flight drag, and a greater potential for encountering shocks on the advancing blade [36], which are factors not addressed in this research. The graph demonstrates that smaller-sized rotors consume considerably more power than larger ones, showcasing a noticeable and substantial decrease in power as the rotor disk diameter increases (also discussed in Refs. [42,43]). Moreover, if the total mass of the aerobot increases, the power required for smaller rotor disks significantly escalates, whereas for larger rotor disk diameters, the power required reaches higher asymptotic values. This difference is demonstrated in the graph comparing a 40 kg to a 20 kg helicopter. Analysing the power requisites, it is apparent that vertical climbing demands slightly more power than hovering, as expected due to the energy needed for vertical forward propulsion. Nevertheless, with increasing rotor disk size, the divergence between the power demands for hovering and climbing becomes more noticeable over time.

Figs. 14 and 15 present graphical representations of hover power and vertical climb power relative to the rotor disk diameter, respectively, across various rotorcraft configurations: conventional helicopter, LS (large separation) coaxial rotorcraft, three tandem rotorcraft cases, and rotorcraft with two isolated rotors. It is worth noting that the extension of power data for two equal isolated rotors beyond a rotor disk size of

Table 4
Parameters and variables used in the forward flight, vertical climb, and hover power analysis of various rotorcraft configurations.

Parameter	Values			Unit
Mars Mean Air Density at SW Melas Basin	0.016			kg/m^3
Average Speed of Sound on Mars	240			m/s
Surface Gravity Acceleration on Mars	3.73			m/s^2
Aircraft MTOG Mass, m_0	20			kg
Aircraft MTOG Weight, W_0	74.60			N
Allowable Maximum Rotor Advancing Blade Tip, M_{at}	0.75			Mach
Air Speed at Max M_{at} on Mars	180			m/s
Traverse Range as per Flight Mission	10			km
Cruise Flight Endurance, E	3.0			min
Cruise Flight Velocity, V	55.56			m/s
Dynamic Pressure at the Cruise Velocity, q	24.69			Pa
Flight Altitude as per Flight Mission	1			km
Vertical Climb Endurance, E	2.00			min
Average Vertical Climb Velocity, V_{climb}	8.33			m/s
Rotor Diameter, D	0.23	to	9.0	m
Rotor Disk Area, S	0.04	to	63.6	m^2
Battery Specific Energy, E_{sb}	230.00			Wh/kg
Measure (or figure) of Merit, M	0.6			
Mechanical efficiency factor, $\eta_{mechanical}$	0.97			
Fuselage downwash adjustment, f	1.06			
Helicopter Power ratio ($P_{tail\ rotor}/P_{rotor}$)	0.18			
Coaxial Power ratio ($P_{second\ rotor}/P_{main\ rotor}$)	1			
System efficiency battery to motor (η_{b2s})	0.9			
Propeller Efficiency, η_p	0.8			
Oswald Efficiency, e	0.5			
Parasitic Drag Area, D/q (Front Area x Drag data)	**Front Area**	**Drag Data**	**D/q**	
D/q Fuselage (radius 0.15 m)	7.1E-02	0.09	6.0E-03	m^2
D/q Tubular Landing 4 legs (0.002 m × 0.03 m, each)	2.4E-04	1.01	2.4E-04	m^2
D/q Unfaired Single Rotor (0.005 m × 0.003 m)	1.5E-05	1.20	1.8E-05	m^2
Downwash Interference Drag Fuselage	7.1E-02	0.02	1.4E-03	m^2
Leakage & Protuberance Drag (15 % Total D/q)			1.2E-03	m^2

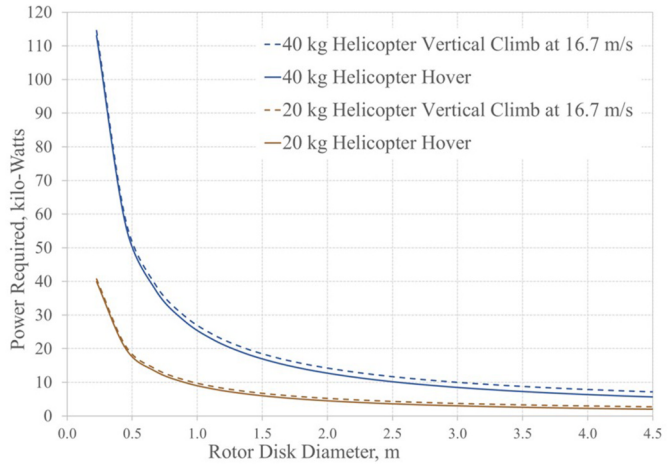

Fig. 13. Power required (Hover & Vertical Climb) vs rotor disk diameter – 20 kg & 40 kg Martian Conventional Helicopter.

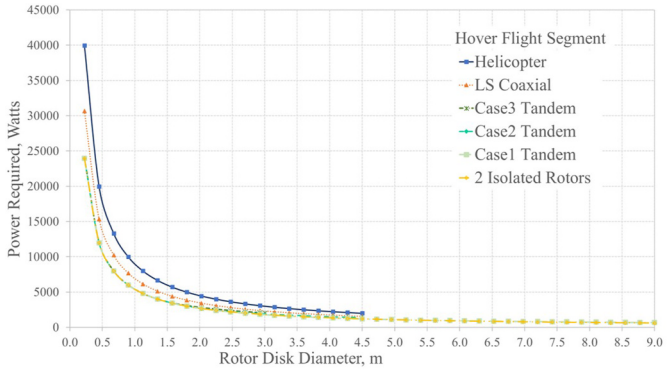

Fig. 14. Power required (Hover) vs rotor disk diameter – Comparison between various 20 kg rotorcraft configurations (Helicopter, Coaxial, Tandem Cases, 2 Isolated Rotors).

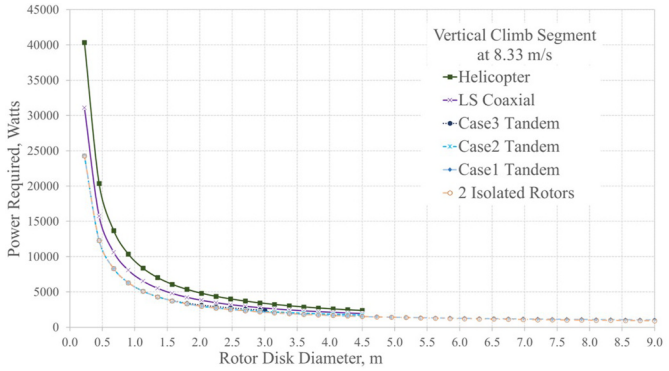

Fig. 15. Power required (Vertical Climb) vs rotor disk diameter – Comparison between various 20 kg rotorcraft configurations (Helicopter, Coaxial, Tandem Cases, 2 Isolated Rotors).

4.5 m is for analytical comparison with tandem rotor Case 1, rather than for practical application. Across all configurations, vertical climbing consistently demands more power than hovering, with this difference progressively increasing as the rotor disk diameter grows. Among these setups, the conventional helicopter exhibits the highest power demand. Conversely, the power consumption of two equal-sized coaxial rotors is lower with smaller-sized rotors, notably at a diameter of 0.23 m, requiring approximately 9,000 Watts less power compared to the conventional helicopter. Similarly, other configurations demand roughly 16,000 Watts less power for both hovering and vertical ascent at this rotor size. At the maximum aeroshell size (corresponding to a rotor diameter of 4.5 m), hover and vertical climb power requirements range approximately between 1,000 and 2,500 Watts for all configurations. In the three tandem rotorcraft cases, it is evident that before rotor overlapping, the power needed aligns with that of isolated rotors. The graphs illustrate a trend where power requirements decrease in inverse proportion to rotor diameter, initially decreasing rapidly and then levelling off as rotor diameter increases. This transition in power requirement becomes insignificant, particularly for tandem rotorcraft Case 1, with rotor disk sizes between 4.5 m and 9 m. Particularly smaller rotor sizes show tandem rotorcraft consuming notably less power than other rotorcraft configurations.

Fig. 16 presents a graph of hover power required by the 20 kg rotorcraft configurations mentioned earlier, plotted against the rotorcraft disk loadings (W/S) on the logarithmic scale (base 2). These data provide insight into the trend in terms of disk loading, whereas earlier Fig. 14 showed hover required power in terms of rotor disk diameter. The nodes or markers on the graph lines indicate the corresponding rotor disk sizes related to the disk loading of the respective rotorcraft, increasing in 5% intervals of the 4.5m aeroshell size, starting at 0.23 m and going up to 9 m (particularly for the 2 isolated rotors and tandem Case 1). Some of these disk sizes are labelled across the graph, particularly the smallest and largest sizes. The helicopter uses a single rotor of mentioned disk size, whereas other rotorcraft use dual rotors of labelled sizes; hence, it is apparent that the helicopter consumes the highest power followed by a coaxial rotor with tandem and isolated rotors. It is well established that the lower disk loading means that less power is required to hover, however, it is interesting to note that for the given rotorcraft weight, the rotorcraft with disk loading under 64 N/m^2 (rotor disk diameter >1 m) require substantially less power when compared to the rotor disk sizes lower than 1 m diameter. The disk loading increases rapidly, from 60 to 2000 N/m^2 (approx.), as the rotor disk diameter reduces from about 1m to 0.23 m, respectively. As shown in the previous graphs, the single-rotor helicopter consumes more power than the coaxial rotorcraft, while the tandem rotorcraft is the most efficient, with the disk loading graph highlighting these differences more prominently for smaller rotors. Similarly, a graph of the power loading (W/P) of these 20 kg rotorcraft configurations during hover is plotted against the rotorcraft disk loading, using log scale (base 2) for both axes for better clarity, as shown in Fig. 17. The more power-efficient the rotorcraft, the higher its power loading, as reflected in the plot, where the tandem and 2 isolated rotorcraft configurations have higher power loading than the coaxial, while the helicopter configuration has the lowest for similar disk sizes. The power loading inversely decreases with an increase in disk loading (appearing as a linear decrease on a log scale), reflecting a reduction in rotor disk size for a given mass.

8.2. *Forward flight analysis*

The analysis shown of a conventional helicopter for Mars in Fig. 18 includes forward-level flight and forward climb flight at a 20-degree climb path angle, flying at a cruise velocity of 55.56 m/s. A trend is apparent in the graph that climbing while flying forward demands higher power compared to straightforward forward flight. However, at smaller rotor disk sizes, both flight modes exhibit similar power consumption, with the difference becoming noticeable at and beyond a rotor disk diameter of about 0.5 m. Unlike levelled flight, the power requirement for forward climb flight does not decrease as significantly with increasing rotor disk size.

Fig. 19 presents a snapshot of the required power for forward levelled flight among the discussed rotorcraft configurations, up to rotor disk sizes of 9 m. Notably, at the smallest rotor disk size, the conventional helicopter demonstrates the highest and unrealistic power demand, followed by the coaxial rotorcraft, tandem rotorcraft cases, and

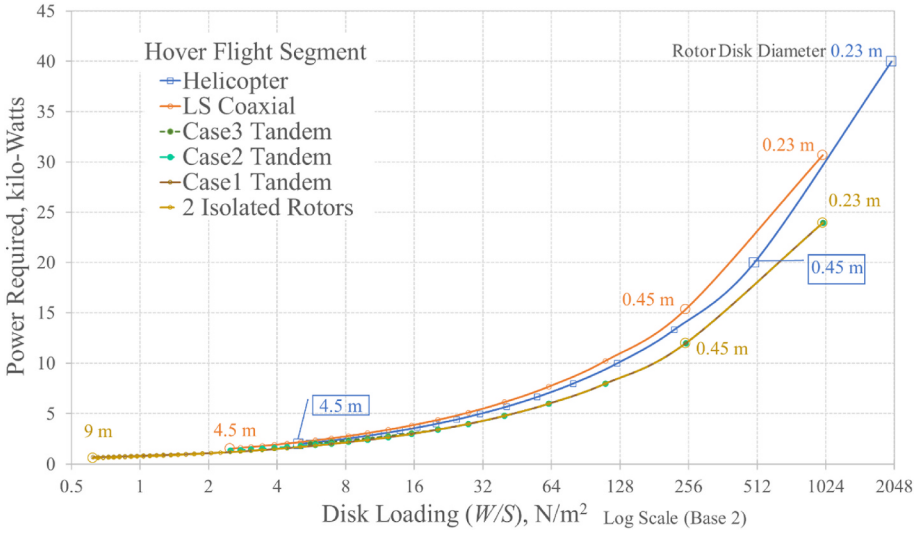

Fig. 16. Power required (Hover) vs disk loading (W/S - on log scale base 2) – Comparison between various 20 kg rotorcraft configurations (Helicopter, Coaxial, Tandem Cases, 2 Isolated Rotors).

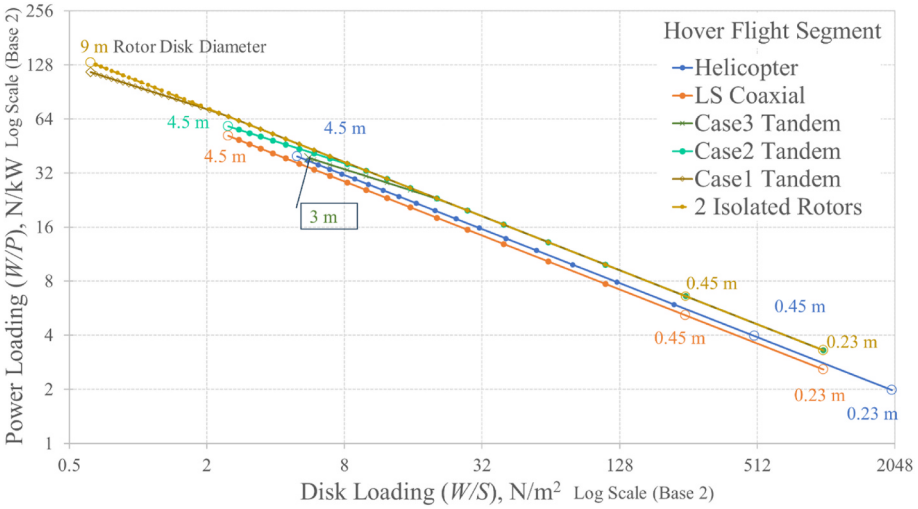

Fig. 17. Power loading (*W/P*) (Hover) vs disk loading (*W/S*) (both axes on Log scale base 2) – Comparison between various 20 kg rotorcraft configurations (Helicopter, Coaxial, Tandem Cases, 2 Isolated Rotors).

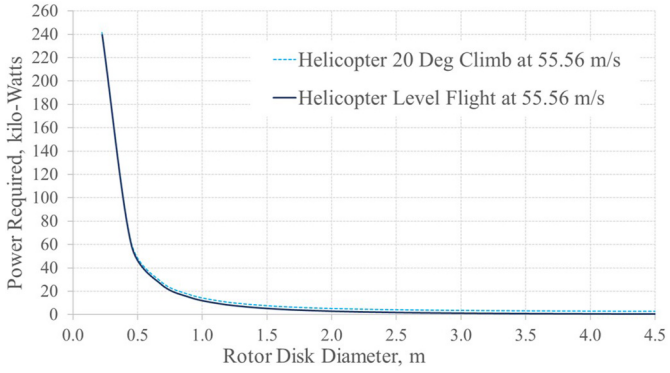

Fig. 18. Power required (Forward Level & Climb Flight) vs rotor disk diameter – 20 kg Martian Conventional Helicopter.

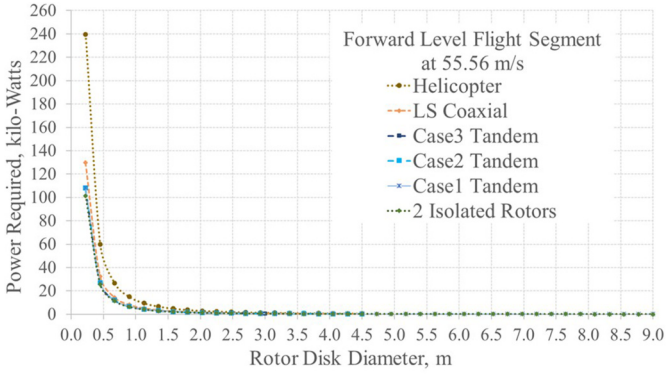

Fig. 19. Power required (Forward Level) vs rotor disk diameter– Comparison between various 20 kg rotorcraft configurations (Helicopter, Coaxial, Tandem Cases, 2 Isolated Rotors).

then the two isolated rotors. However, with a slight increase in rotor disk size, the power requirement dramatically decreases, until the reduction in power becomes negligible from a rotor size of about 2 m onward.

Fig. 20 displays a detailed observation of the power differences among various rotorcraft configurations for both forward level and climb flights, setting the rotor disk diameter from 1 m on the horizontal axis. During the forward climb of tandem rotorcraft Case 1, a notable observation arises: after initially reaching a minimum, the required power begins to increase as the tandem rotors start to overlap beyond a rotor diameter of 4.5 m, influenced by the introduction of an additional overlapping interference factor (K_{ov}) in conjunction with the downwash factor (K_{dw}). A similar trend is noted with Case 2 tandem rotorcraft but only at the upper limit of the rotor diameter.

It is apparent that beyond rotor disk sizes of 3 m, except for the helicopter, all other rotorcraft configurations for forward level flight require around or under 1000 Watts of power. Conversely, for forward flight at a 20-degree climb angle, the power requirement ranges from approximately 2500 to 3500 Watts. Although climbing while flying forward demands more power than levelled flight, achieving height during forward flight is more energy efficient than vertical flight overall. Flying closer to the ground, known as ground effects, creates an air cushion under the aircraft, aiding in reaching optimal flight speed before ascending, thus reducing energy losses. This analysis is performed below the maximum allowed forward flight speed (60 m/s, refer to subsection 4.3) to prevent air shock buildup at the rotor tip speed; however, if we experiment with increasing the forward speed further, the required forward flight power will decrease. Additionally, a lower climb path angle would result in less power required for forward climb flight.

Fig. 21 presents a graph depicting the power required for forward level flight by the 20 kg rotorcraft configurations, plotted against rotorcraft disk loading (W/S) on logarithmic scale (base 2). This analysis parallels the hover power analysis shown in Fig. 16. While Fig. 19 illustrated the power requirements for forward level flight as a function of rotor disk diameter, this data provides insight into the trends relative to disk loading. It is apparent from this disk loading graph that for smaller rotor sizes, helicopter configuration becomes significantly more inefficient during cruise than in hover when compared to other configurations. Additionally, the tandem configuration consumes more power during the forward flight compared to the ideal two isolated rotors, a contrast to the hover segment shown in Fig. 16. This loss in performance is attributed to the downwash interference experienced by the rear rotor from the wake of the front rotor, as described in Eq. (12). Similarly, Fig. 22 shows a graph of the forward level flight power loading (W/P) of these 20 kg rotorcraft configurations plotted against the rotorcraft disk loading using logarithmic scale (base 2) for both axes for better clarity. The trends observed are similar to the hover power loading graph (Fig. 17) such that the helicopter has the lowest power loading, followed by coaxial rotorcraft, tandem and then the rotorcraft with the 2 isolated rotors.

Fig. 23 illustrates the relationship between power required and rotor disk diameter for three rotorcraft configurations (Helicopter, LS Coaxial, and Case 1 Tandem) operating in Martian atmospheric conditions at two densities, 0.013 kg/m^3 and 0.025 kg/m^3. These density values account for seasonal and altitude-based variations discussed in Section 4.1, with the lower density corresponding to the primary mission location at SW Melas Chasma during the summer season and the higher density reflecting the secondary mission location approximately 2000 km lower in elevation during winter. The data corresponds to forward level flight at a velocity of 55.56 m/s. Across all configurations, the power required decreases as rotor disk diameter increases, driven by improved aerodynamic efficiency resulting from reduced disk loading with larger rotor sizes. The Helicopter configuration consistently demonstrates the highest power requirements, particularly under the lower density condition of 0.013 kg/m^3, highlighting its relatively lower efficiency. In contrast, the LS Coaxial configuration shows improved efficiency over the Helicopter, while the Case 1 Tandem configuration is the most efficient, requiring the least power across all densities and rotor diameters. Atmospheric density significantly impacts power requirements, influenced by both seasonal and altitude-based variations. Higher density (0.025 kg/m^3) reduces power consumption for all configurations due to enhanced aerodynamic lift efficiency, with this effect being more pronounced for smaller rotor diameters. At larger rotor diameters (above 3 m), power requirements across all configurations converge, reflecting diminishing differences in efficiency. The graph highlights the tandem configuration's superior power efficiency, particularly in low-density Martian conditions, while emphasising the critical influence of rotor disk diameter on aerodynamic performance. These findings underscore the importance of optimising rotor size and configuration to meet mission-specific requirements under varying Martian atmospheric conditions influenced by both seasonality and altitude.

8.3. Battery mass fraction (BMF) analysis

Fig. 24 illustrates the Battery Mass Fraction (*BMF*) concerning the vertical climb required power across various defined rotorcraft configurations, demonstrating its correlation with increasing rotor disk

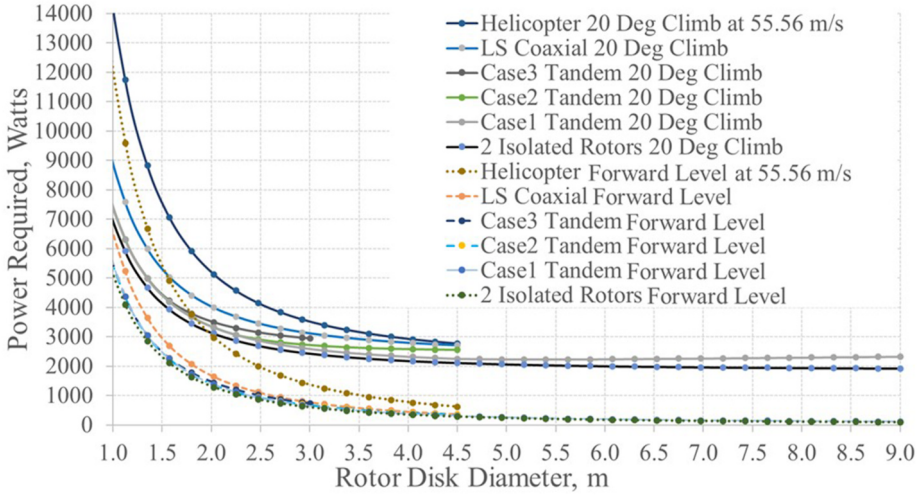

Fig. 20. Power required (Forward Level & Climb Flight at 55.56 m/s) vs rotor disk diameter (Rotor Diameter Limits - 1 to 9 m) – Comparison between various 20 kg rotorcraft configurations (Helicopter, Coaxial, Tandem Cases, 2 Isolated Rotors).

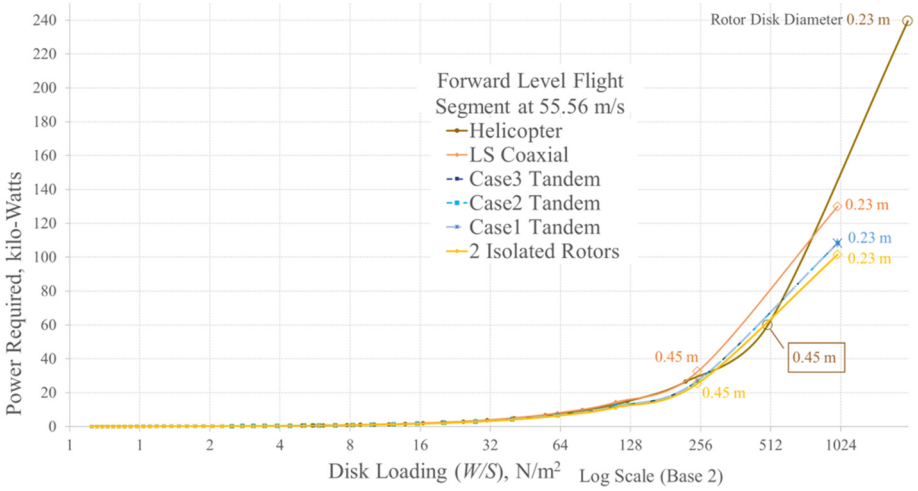

Fig. 21. Power required (Forward Level Flight) vs Disk Loading (W/S) – Comparison between various 20 kg rotorcraft configurations (Helicopter, Coaxial, Tandem Cases, 2 Isolated Rotors).

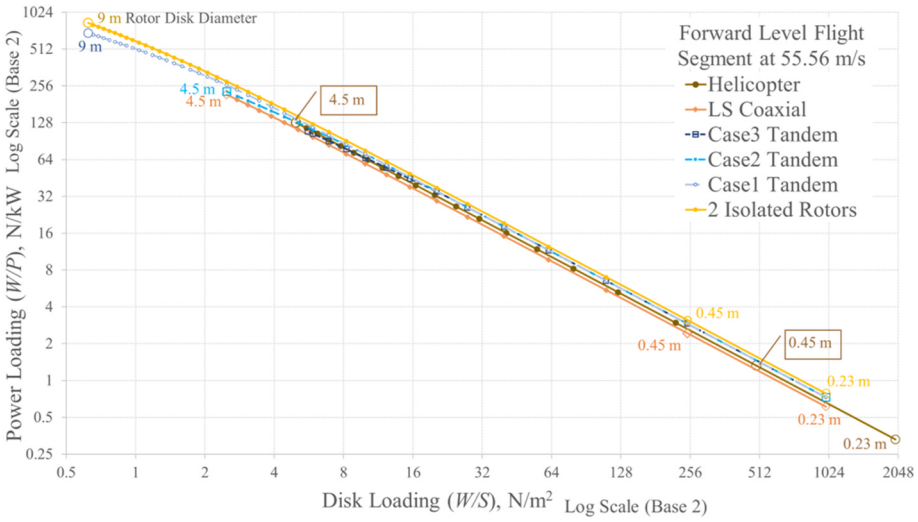

Fig. 22. Power loading (*W/P*) (Forward Level Flight) vs disk loading (*W/S*) (both axes on Log scale base 2) – Comparison between various 20 kg rotorcraft configurations (Helicopter, Coaxial, Tandem Cases, 2 Isolated Rotors).

diameter. This *BMF* calculation, using Eq (14), considers a 2-min run time (*E*), a climb speed of 8.33 m/s, and a constant total mass of 20 kg. The trend observed in the vertical climb *BMF* lines aligns with the vertical climb power dependency outlined in Fig. 15. Essentially, as the required power increases, the *BMF* also increases, indicating the necessary battery weight for this specific flight segment. A similar *BMF* trend is observed for the forward-level flight segments depicted in Fig. 25, mirroring the forward-level flight power data from Fig. 19. The required battery mass can simply be determined by multiplying the total *BMF* by the total aircraft mass. For instance, with a 0.03 BMF, the battery mass would equal 0.6 kg (i.e., 0.03 × 20 kg). It is essential to aggregate the *BMF* of each segment with the BMF of other flight segments, as detailed in Section 6, to ascertain the total *BMF* and thus determine the overall battery mass necessary for a specific flight regime. Moreover, it is noteworthy that the *BMF* calculated for the flight mission excludes the battery mass required for avionics or electronic payload instruments. Separate calculations would be needed for these unless these have dedicated batteries of their own.

9. Practical application of the analysis and discussion

This penultimate section presents the concluding steps of the framework for the preliminary design of future rotary VTOL Martian aerobots (Fig. 1), applied in this research through an example case study in a systematic manner. The initial sizing method (step 9 within the framework) for the battery electric aircraft, introduced in Section 6, is conducted on the designs shortlisted based on power efficiency and specific design constraints discussed in the subsequent subsection. While the calculation of the aerobot's empty mass by specifying structural materials and subsystem components (step 10) is introduced here, the detailed execution of this step is beyond the scope of this paper, as mentioned in the introduction of the framework.

9.1. *Efficient rotor configuration shortlisting*

Based on the power requirement analysis of rotorcrafts with single and dual rotors, the lowest power-consuming rotorcraft configurations can be shortlisted for the aerobot design. However, specific design constraints are established to exclude certain theoretical findings that may seem optimal in theory but introduce design complexities,

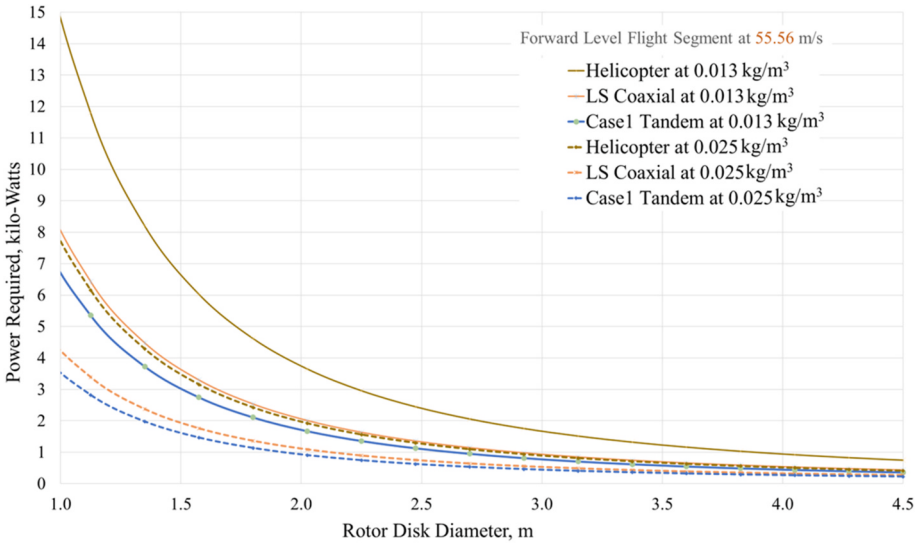

Fig. 23. Power required (Forward Level) vs rotor disk diameter (1–4.5 m)– Comparison between various 20 kg rotorcraft configurations (Helicopter, Coaxial and Tandem Case1) at 0.013 kg/m^3 and 0.025 kg/m^3.

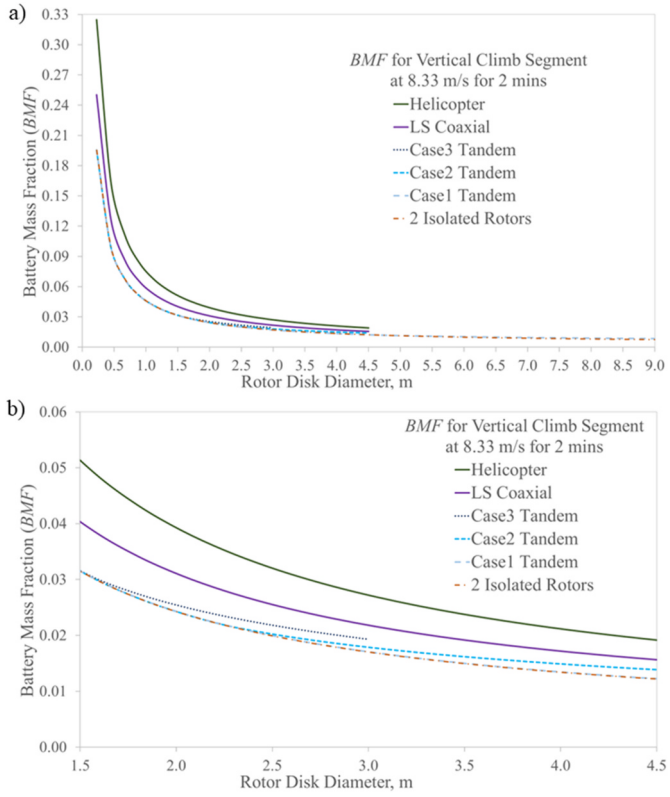

Fig. 24. BMF vertical climb segment (at 8.33 m/s for 2 min) vs rotor disk diameter– Comparison between various 20 kg rotorcraft configurations (Helicopter, Coaxial, Tandem Cases, 2 Isolated Rotors). a) Shows *BMF* for rotor diameters from 0 to 9 m on the x-axis. b) Shows a zoomed-in view, focusing on *BMF* for rotor diameters from 1.5 to 4.5 m on the x-axis for clarity.

including folding and stowing requirements, the need for heavy and robust materials, as well as control and stability concerns, exemplified by the 9 m rotor diameter of the Case 1 Tandem rotorcraft. Similarly, smaller-sized rotors, while lighter and mechanically simpler, demand higher power and are more suitable for small to medium-sized multicopters rather than large helicopters or rotorcrafts. Therefore, Fig. 26 presents a zoomed-in view of the analytical graphs comprising the

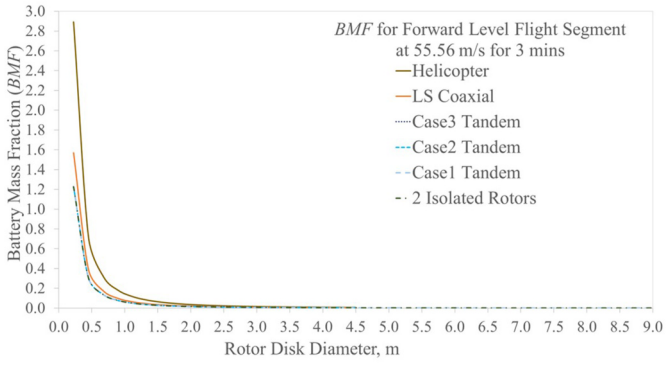

Fig. 25. BMF forward level flight segment (at 55.56 m/s for 3 min) vs rotor disk diameter – Comparison between various 20 kg rotorcraft configurations (Helicopter, Coaxial, Tandem Cases, 2 Isolated Rotors).

power required for vertical climb and level forward flight against the rotor disk diameter with limits set from 1.5 m to 4.5 m. As per the basic mission flight profile (Fig. 12), the rotorcraft must ascent vertically and cruise forward. Conventional helicopter within the set parameters consumes the highest power for both flight segments and therefore can rationally be omitted. The lowest power is required by Case 1 Tandem rotorcraft and then by Case 2, but both require a rotor folding mechanism and potentially a heavier articulated hub system as mentioned in Table 3 (for Case 2, when $D > 2.25$). One of the important factors in designing a rotorcraft for an extraterrestrial application is keeping the operational capability as simple as possible to minimize any malfunction risk because maintenance or mechanical error correction by physical means is not possible. Thus, these two tandem rotorcraft cases are deprioritised. Case 2 of tandem rotorcraft with a rotor diameter of $D <$ 2.25 fits inside the aeroshell vessel without requiring any folding mechanism, while its rotors present the more efficient isolated behaviour due to the absence of overlapping. When doing trade-offs based on the complexity, weight and maintenance factors, such configurations are likely to be prioritised.

Coaxial rotorcraft with large separation (LS) between rotors and Case 3 Tandem rotorcraft are the remaining choices. The overlapping interference factor (K_{ov}) for LS coaxial rotors is 1.281, while for Case 3 tandem rotorcraft at a maximum allowable rotor diameter of 3 m (resulting in a maximum tandem rotor overlapping), the K_{ov} is 1.134.

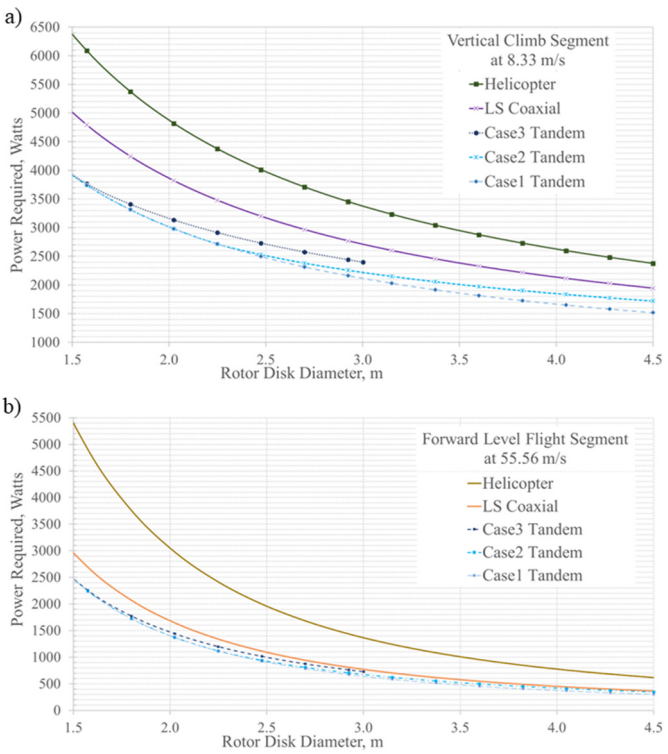

Fig. 26. Power required [Graph a) vertical climb at 8.33 m/s. graph b) level forward flight at 55.56 m/s] vs rotor disk diameter (rotor diameter range - 1.5m–4.5m) – Comparison between various 20 kg rotorcraft configurations (Helicopter, Coaxial, Tandem Cases).

The K_{ov} of Case 3 is lesser for rotor disks smaller than 3 m in diameter due to a decrease in rotor overlapping. A noticeable difference of around 1000 Watts is evident between the two configurations for vertical climb power at a rotor diameter of 1.5 m, where the tandem rotor shows zero overlapping in this instance. Whereas, for a forward levelled flight the difference at 1.5 m disk size is about 400 Watts, which keeps becoming negligible with the increase in rotor size. Consequently, tandem rotor Case 3 emerges as a favourable configuration option, displaying higher hover and vertical climb power efficiency compared to the LS coaxial setup. Additionally, it is mechanically less complex than other tandem cases, owing to the capability of using a rigid rotor hub system. For rotor disk sizes beyond 3 m, LS coaxial rotors could be an option, albeit with a higher K_{ov} trade-off. Moreover, this simplified calculation for K_{ov} of tandem rotorcraft is based on the same plane rotors overlapping, but in the practical designs, the rear rotor is placed at a greater height than the front rotor to minimize the interference effects of the front rotor wake. Thus, the K_{ov} would be further reduced and hence, also the required power.

9.2. Initial sizing application and battery considerations

Case 3 Tandem rotorcraft with a 3 m rotor disk size is selected for preliminary study as an example (Fig. 27). As mentioned in Section 7.2, the battery-specific energy (E_{sb}) used for Battery Mass Fraction (*BMF*) calculations for flight is 230 Wh/kg pack (including battery management system), based on a JPL technology forecast for next-generation Mars Science Helicopter. The usable energy is 70% of the nominal capacity (10%–80% depth-of-discharge) with an average discharge efficiency of 90% [5]. It is established from the results obtained that the power required at a vertical climb segment is 2400 Watts and at a cruise segment is 730 Watts, and the relative Battery Mass Fraction (*BMF*) is 0.019 and 0.008, respectively. The total *BMF* sums up to 0.027. As explained in Section 6, the nominal usage and discharge efficiency correction factors, totaling 1.4 (1.3 for 70% usable capacity and 1.1 for 90% averaged discharge efficiency deduced in Ref. [5]), are applied to adjust the total BMF. The adjusted BMF is now 0.038. As it is predetermined, the total aerobot mass is set at 20 kg. Therefore, using Eq. (14) the battery mass (m_b) required for this 5-min flight mission is calculated to be around 0.76 kg. Also, it is predetermined that the aerobot should potentially be capable of carrying a science payload of 2 kg. Using Eq. (15) in terms of Mass, the available aircraft's empty mass ($m_e = m_0 - m_b - m_{payload}$) is determined to be 17.24 kg, representing ~86% of the total aircraft mass, a feasible starting point for further analysis.

While the above calculations provide a foundation, further review of available battery technologies is necessary to ensure the design meets the mission's power demands. The battery selection must consider not only energy capacity but also the maximum discharge current capability. The JPL forecast assumes a 10C discharge rate [5], allowing the battery to discharge at ten times its nominal capacity, fully depleting in just 1/10th of an hour. This high discharge capability is essential for intense power phases, such as vertical climb, where sustained delivery of 2400 W is required. To further evaluate the feasibility of the tandem rotorcraft design, the state-of-the-art INR-21700-P50B lithium-ion battery [44] is used as a reference for system configuration. This battery has a nominal voltage of 3.6 V, a capacity of 5 Ah (cell-specific energy 260 Wh/kg), a maximum continuous discharge current of 60 A (C-rate 12C), and a weight of 71 g per cell. By comparison, the Ingenuity helicopter used six Sony SE US18650 VTC4 cells with a nominal voltage of 3.6 V, a capacity of 2 Ah, an energy density of 144 Wh/kg, and a weight of 45 g per cell. The VTC4 cells have a higher C-rate (15C vs. 12C), but the INR-21700-P50B offers over twice the capacity and significantly higher energy density, enabling greater flight durations and improved efficiency.

Two battery configurations are examined: a 6-cell system (21.6 V)

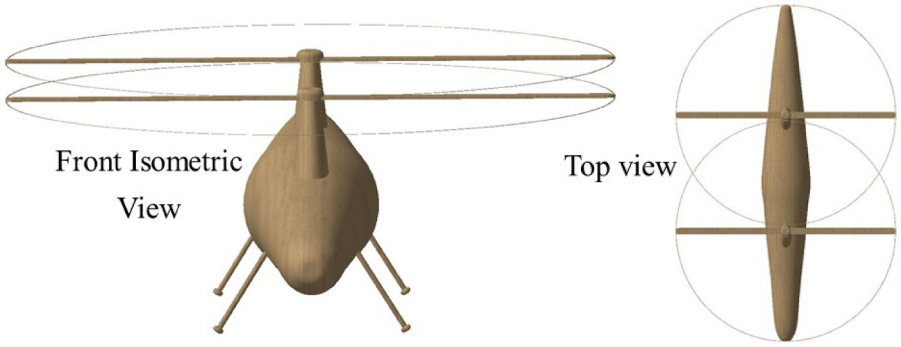

Fig. 27. Case 3 Tandem rotorcraft with a 3 m rotor disk size based on initial sizing (CAD model illustration: the left side is a front isometric view and the right side is a top view. Not to scale).

and a 14-cell system (50.4 V). The 6-cell system, with its lower voltage, results in a higher current demand during vertical climb. Using the relationship, $current = power/(voltage \times efficiency)$, at 2400 W and an efficiency of 90%, the current demand is approximately 123.5 A. This exceeds the 60 A discharge limit of a single cell, necessitating three parallel connections. The total number of cells required for this configuration is 18, with a corresponding battery mass of 1.278 kg. In contrast, the 14-cell system's higher voltage reduces the current demand to 52.9 A, which is within the discharge limit of a single cell. This eliminates the need for parallel connections, reducing complexity and total cell count. With 14 cells in series, the battery mass is 0.99 kg, significantly lighter than the 6-cell configuration and closer to 0.76 kg battery mass calculated earlier using the *BMF* method. The simplified design of the 14-cell system also reduces the need for a complex battery management system, improving reliability and operational efficiency.

Despite the clear advantages of the 14-cell system, the reliance on a 12C discharge rate presents significant challenges. High discharge rates generate substantial heat, requiring advanced thermal management systems to prevent overheating. Sustained high-current operations accelerate chemical degradation, reducing the battery's operational life and limiting mission longevity [5]. Additionally, the energy density of 230 Wh/kg, while high for current lithium-ion technology, restricts mission durations and payload capacity. The harsh Martian environment further complicates performance; low temperatures increase internal resistance, degrading battery efficiency and requiring additional heating systems, which consume energy and add mass.

Addressing these challenges will require advancements in battery technology. Selecting appropriate battery technology is crucial for Mars missions due to the planet's extreme conditions. Lithium-ion (Li-ion) batteries are widely used in space missions for their high energy density and reliability; for instance, NASA's Mars Exploration Rovers, Spirit and Opportunity, utilised rechargeable lithium-ion batteries to store energy generated from their solar panels, enabling operations during periods without sunlight. Lithium polymer (LiPo) batteries offer high discharge rates and flexible form factors but generally have lower energy densities and are more susceptible to swelling and thermal runaway under extreme conditions, making them less suitable for the harsh Martian environment. Lithium iron phosphate ($LiFePO_4$) batteries are known for excellent thermal and chemical stability, enhancing safety and longevity; however, their lower energy density can be a disadvantage in weight-sensitive space applications. Emerging technologies like solid-state batteries, which utilise solid electrolytes, offer higher energy densities and improved safety profiles due to resistance to leakage and thermal runaway. They are being developed to operate effectively in extreme environments, including the temperature fluctuations on Mars. Furthermore, optimising the aerobot's mission profile to reduce power demand during critical phases, such as vertical climb, could help lower current requirements, simplifying the overall battery configuration.

In Section 6 the contents included in empty mass are described, and calculating the total mass of such components is a detailed process based on further design requirements (step 10, Fig. 1). For initial estimation, the mass of commercially available off-the-shelf (COTS) materials and components can be used. Alternatively, aircraft mass buildup can be evaluated by referencing the mass specifications of similar aircraft, such as the weight estimation model for second-generation Mars Science Helicopters in Ref. [5], which is based on the first Mars Helicopter.

9.3. Discussion

The primary aim of this parametric study is to provide a theoretical baseline using existing helicopter momentum theory to estimate power consumption for different rotorcraft configurations in Martian conditions. Given the early stage of this research, this fundamental approach focuses on understanding performance requirements for rotorcraft flight on Mars, similar to the use of blade element momentum theory in the conceptual design process of NASA's Mars helicopters [5]. However, the derivative method introduced here includes flight performance analysis of both overlapping and non-overlapping rotors, allowing effective exploration of a wide range of configurations and parameters, establishing baseline estimates and comparative analyses. The results obtained from the parametric performance study conducted on rotorcraft with single and dual rotors, are reasonable within the framework of the momentum theory and include refinements based on insights from previous publications by the authors. Adjustments have been made to parameters such as the figure of merit, fuselage downwash interference factor, and Oswald's efficiency factor to suit Martian conditions. This methodology can be extended to include multirotor configurations, including quadrotors and hexarotors [45].

The initial sizing method applied in the preceding subsection assumed fixed values for payload mass and total rotorcraft mass to initiate the sizing process. However, while payload mass serves as a criterion for setting requirements, it can alternatively be integrated into the empty mass of the rotorcraft such that the total mass equals battery mass and empty mass ($m_0 = m_b + m_e$). This approach allows flexibility in adjusting payload mass because different rotorcraft configurations necessitate varying airframe and motor masses. Consequently, a heavier structure can accommodate a lighter payload, and vice versa, ensuring that the total rotorcraft mass remains constant. If the payload mass is predefined and fixed, adjustments in the total mass are essential depending on the calculated empty mass. Nevertheless, the next critical step in the preliminary design framework is the detailed mass buildup process (step 10, Fig. 1), as it accounts for factors such as rotor, propulsion and energy system mass adjustments based on rotor efficiency and changes in airframe mass according to configuration.

The tandem rotor configuration was selected for its power efficiency and mechanical simplicity, particularly in scenarios requiring higher payload capacities and extended endurance. This design offers advantages over single and coaxial rotors by distributing the aerodynamic load across two rotor disks with partial overlapping, thereby reducing individual disk loading and optimising power requirements. However, tandem configurations introduce significant aerodynamic challenges, including wake interactions between the front and rear rotors. These wake effects can impact the overall aerodynamic efficiency, increase vibration levels, and complicate flight stability and control. Managing the aerodynamic interactions in a tandem rotor system requires sophisticated control strategies to maintain desired flight characteristics [46], especially in the thin Martian atmosphere where aerodynamic behaviours differ significantly from Earth's.

Given the unique challenges and high costs associated with Martian rotorcraft experimentation, the framework proposed in this research for the preliminary rotorcraft design, coupled with theoretical analytical methodology, serves as a crucial first step in a broader validation process. Future work involves refining the performance estimates of shortlisted rotorcraft configuration/s using advanced methodologies like blade element theory, vortex wake models or Computational Fluid Dynamics (CFD), alongside considerations of fuselage wake interaction and drag, to provide more precise estimates of battery mass and overall aerodynamic performance. Moreover, detailed assessments of rotor efficiency in forward flight become essential at high advance ratios where advancing blade tip speeds reach near-Mach numbers. These conditions introduce compressibility effects and altered aerodynamics, influencing rotor performance significantly. Thus, addressing these factors will be key to advancing the reliability and applicability of rotorcraft designs for Martian exploration.

10. Conclusion

The successful flight of the first Mars Helicopter has shown the potential for rotorcraft flight on the red planet. The systematic methodology for the preliminary design of future rotary VTOL Martian aerobots was proposed and applied within a structured framework in this research using an example case study. The detailed analysis reveals the

critical importance of an aerobot in exploring Mars' Southwestern Melas Basin in Valles Marineris, showcasing the complex mission planning required for successful Martian exploration. To pave the way for future Mars rotorcraft, this study addressed critical research gaps by defining essential parameters and conducting a comprehensive parametric analysis of various 20 kg rotorcraft configurations with single and dual rotors. Using simplified helicopter momentum theory equations, the power requirements for hover, vertical climb, and forward flight concerning varying rotor disk diameters for diverse rotorcraft types were illustrated through graphical representations, revealing that conventional helicopters consume more power than other configurations under given parameters. Rotorcraft with two isolated rotors stand out due to the non-overlapping aerodynamic interference. Notably, as rotor disk diameter approaches the upper size limit, differences in power requirements among configurations become negligible. The paper outlines methodologies for sizing battery-electric aircraft and calculating Battery Mass Fractions for different flight segments to determine the required battery mass. The analysis of rotorcraft configurations led to the prioritisation of the Case 3 Tandem rotorcraft as an example for further feasibility assessments, due to its higher power efficiency and mechanical simplicity. Initial sizing calculations confirm its feasibility, presenting an available empty mass of 17.24 kg, marking a plausible starting point for subsequent design evaluations and developments. The proposed framework for preliminary rotorcraft design, combined with a theoretical and analytical methodology extendable to other multirotor configurations, serves as a crucial first step in a broader validation process for Martian rotorcraft given the unique challenges and high costs of experimentation. Future studies should address data limitations and explore environmental influences on rotorcraft performance for continued progress in Martian exploration.

CRediT authorship contribution statement

Vishal Youhanna: Writing – original draft, Visualization, Validation, Software, Project administration, Methodology, Investigation, Formal analysis, Data curation, Conceptualization. **Leonard Felicetti:** Writing – review & editing, Supervision, Project administration. **Dmitry Ignatyev:** Writing – review & editing, Supervision, Resources, Project administration.

Declaration of competing interest

The authors declare that they have no known competing financial interests or personal relationships that could have appeared to influence the work reported in this paper.

Acknowledgements

The authors would like to express their sincere gratitude to Dr Wayne Johnson (NASA Ames Research Center), for the invaluable feedback and constructive comments, which have contributed to the improvement of the analysis in this paper.

Data availability

Data supporting this study are included within the article and/or supporting materials.

References

[1] M. Hassanalian, D. Rice, A. Abdelkefi, Evolution of space drones for planetary exploration: a review, Prog. Aero. Sci. 97 (2018), https://doi.org/10.1016/J.PAEROSCI.2018.01.003, 2018. 61–2018.105.
[2] NASA. Mars Helicopter - NASA Mars. Retrieved July 20, 2024, from https://mars.nasa.gov/technology/helicopter/#Flight-Log.
[3] NASA. Overview. Mars - NASA Solar System Exploration. Retrieved November July 20, 2024, from https://solarsystem.nasa.gov/planets/mars/overview/.
[4] M. Radotich, S. Withrow-Maser, Z. deSouza, S. Gelhar, H. Gallagher. (2021). A study of past, present, and future mars rotorcraft, 9th Biennial Autonomous VTOL Technical Meeting, Retrieved December 22, 2024. https://ntrs.nasa.gov/citations/20210000448.
[5] W. Johnson, S. Withrow-Maser, L. Young, C. Malpica, W.J.F. Koning, W. Kuang, M. Fehler, A. Tuano, A. Chan, A. Datta, C. Chi, R. Lumba, D. Escobar, J. Balaram, T. Tzanetos, H. Fjaer Grip. (2020) Mars science helicopter conceptual design, Retrieved December 22, 2024. https://ntrs.nasa.gov/api/citations/20200002139/downloads/1405_Johnson_Final_080420[1].pdf.
[6] L.A. Young, R.T.N. Chen, E.W. Aiken, G.A. Briggs. (2000). Design opportunities and challenges in the development of vertical lift planetary aerial vehicles, in: Proceedings of the American Helicopter Society International Vertical Lift Aircraft Design Specialist's Meeting, Retrieved December 22, January 2024. https://rotorcraft.arc.nasa.gov/Publications/files/Young_AHS_Design2000.pdf.
[7] C. Underwood, N. Collins, Design and control of a Y-4 tilt-rotor VTOL aerobot for flight on mars. Proceedings of the 68th International Astronautical Congress (IAC), 2017, pp. 25–29. https://openresearch.surrey.ac.uk/esploro/outputs/conferencePresentation/Design-and-Control-of-a-Y-4-Tilt-Rotor-VTOL-Aerobot-for-Flight-on-Mars/99511131102346.
[8] J. Aguirre, V. Casado, N. Chamie, G. Zha, Mars intelligent reconnaissance aerial and ground explorer (MIRAGE) AIAA 2007-244. https://doi.org/10.2514/6.2007-244, 2007.
[9] J. Forshaw, V. Lappas, Architecture and systems design of a reusable Martian twin rotor tailsitter, Acta Astronaut. 80 (0) (2012) 166–180, https://doi.org/10.1016/J.ACTAASTRO.2012.05.008.
[10] NASA, NASA TechPort - mars electric reusable flyer - project data, Retrieved July 20, 2024, from, https://techport.nasa.gov/view/93850, 2018.
[11] R.N.J. Boelhouwer, E.C. Bunschoten, C.M.J. Debusscher, W. Frijters, R.J. van Goeverden, E.B. Legrand, J. Matton, K. Paliusis, J.K.N. Verheyen, Design Report, Martian Advanced Reconnaissance System, Delft University of Technology, 2018. June 2018.
[12] RM Zubrin, The mars gashopper - concepts and approaches for mars 2012. https://ui.adsabs.harvard.edu/abs/2012LPICo1679.4069Z/abstract, 2012.
[13] Denys, K. Ukrainian invention to feel the ground for Mars colonization (GRAPHICS) - Jun. 06, 2016 | KyivPost. Retrieved July 20, 2024, from https://www.kyivpost.com/article/content/ukraines-it-edge/ukrainian-invention-to-feel-the-ground-for-mars-colonization-graphics-415570.html.
[14] M. Fathepure, A.L. Booker, O. Abouzahr, N. Wang, D. Tikalsy, Design and construction of an inflatable-winged VTOL mars electric flyer, in: AIAA AVIATION 2021 FORUM, 2021, p. 2578, https://doi.org/10.2514/6.2021-2578.
[15] N. Schatzman, M. Dominguez, P. Lee, L. Young, LILI (Long-term ice-field levitating investigator): mars aerial and ground explorer for Martian polar regions. Aeromechanics for advanced vertical flight technical meeting, transformative vertical flight 2022, in: NASA Technical Reports Server, 2022. Retrieved December 15, 2024, from, https://ntrs.nasa.gov/citations/20210026216.
[16] S. Withrow-Maser, W. Johnson, L. Young, H. Cummings, A. Chan, T. Tzanetos, J. Balaram, Bapst, An advanced mars helicopter design. Accelerating Space Commerce, Exploration, and New Discovery Conference, ASCEND, Virtual Event, 2020. https://doi.org/10.2514/6.2020-4028. November 16-18.
[17] L. Sopegno, S. Martini, S. Pedone, A. Fagiolini, M.J. Rutherford, M. Stefanovic, A. Rizzo, P. Livreri, K.P. Valavanis, An advanced hexacopter for mars exploration: attitude control and autonomous navigation, IEEE Trans. Aero. Electron. Syst. (2024), https://doi.org/10.1109/TAES.2024.3365667.
[18] V. Zappek, M. Rinker, L. Daxer, M. Hajek, Evaluation of aerial vehicle configurations for high-range Mars missions, CEAS Space J. 15 (2023) 761–775, https://doi.org/10.1007/s12567-022-00479-4.
[19] B. Lou, X. Yan, P. Zhao, A. Xie, D. Zhang, S. Zhu, Preliminary design of several new kinds of Martian aircrafts. Proceedings of the Vertical Flight Society's 77th Annual Forum & Technology Display, 2021, https://doi.org/10.4050/F-0077-2021-16736.
[20] M.B. Hazarika, G. Santangelo, M. Gamba, W. Wang, Development of a preliminary design methodology for rotorcrafts in Martian atmospheric conditions and experimental validation of the method. https://doi.org/10.2514/6.2023-4802, 2023, October 17.
[21] V. Youhanna, L. Felicetti, D. Ignatyev, Parametric analysis of rotary VTOL aerobot design configurations to fly on Titan, in: 75th International Astronautical Congress IAC-2024, 2024, pp. 14–18. October 2024, Milan, Italy Retrieved December 22, 2024, from, https://dspace.lib.cranfield.ac.uk/handle/1826/23153.
[22] J.A. Grant, M.P. Golombek, S.A. Wilson, K.A. Farley, K.H. Williford, A. Chen, The science process for selecting the landing site for the 2020 Mars rover, Planet. Space Sci. 164 (2018) 106–126, https://doi.org/10.1016/J.PSS.2018.07.001.
[23] C. Cockell, J. Bridges, L. Dannatt, M. Burchell, M. Patel, M. Danson, Where to land on Mars, Astron. Geophys. 50 (6) (2009) 6.18–6.26, https://doi.org/10.1111/J.1468-4004.2009.50618.X.
[24] Banfield et al Mars Science Goals, Objectives, Investigations, and Priorities: 2020 Version Mars Exploration Program Analysis Group (MEPAG) Prepared by the MEPAG Goals Committee. Retrieved July 20, 2024, from https://mepag.jpl.nasa.gov/reports/MEPAGGoals_2020_MainText_Final.pdf.
[25] K.A. Farley, K.H. Williford, K.M. Stack, R. Bhartia, A. Chen, M. de la Torre, K. Hand, Y. Goreva, C.D. Herd, R. Hueso, Y. Liu, J.N. Maki, G. Martinez, R. C. Moeller, A. Nelessen, C.E. Newman, D. Nunes, A. Ponce, N. Spanovich, Y. Liu, Mars 2020 mission overview, Space Sci. Rev. (2020), https://doi.org/10.1007/s11214-020-00762-y.
[26] NASA. Location Map for Perseverance Rover - NASA Mars. Retrieved July 20, 2024, from https://mars.nasa.gov/mars2020/mission/where-is-the-rover/.

[27] NASA.Vallis Marineris. Retrieved July 20, 2024, from https://web.archive.org/web/20070711145413/http:/education.gsfc.nasa.gov/experimental/all98invProject.Site/Pages/Vallis.Marineris.html.
[28] Christensen, P.R.; Engle, E.; Anwar, S.; Dickenshied, S.; Noss, D.; Gorelick, N.; Weiss-Malik, M.; JMARS – A Planetary GIS, http://adsabs.harvard.edu/abs/2009AGUFMIN22A..06C.
[29] JOUAV, Top 10 drones with the longest flight time in 2023 - JOUAV, Retrieved July 20, 2024, from, https://www.jouav.com/blog/drone-with-longest-flight-time.html, 2023.
[30] J. Balaram, M. Aung, M.P. Golombek, The ingenuity helicopter on the perseverance rover, Space Sci. Rev. 217 (4) (2021) 56, https://doi.org/10.1007/s11214-021-00815-w.
[31] NASA, Hazard: distance from Earth - NASA, Retrieved July 20, 2024, from, https://www.nasa.gov/hrp/hazard-distance-from-earth/, 2024.
[32] NASA, Mars fact sheet, Retrieved July 20, 2024, from, https://nssdc.gsfc.nasa.gov/planetary/factsheet/marsfact.html.
[33] NASA, Mars atmosphere model - metric units, Retrieved July 20, 2024, from, https://www.grc.nasa.gov/www/k-12/airplane/atmosmrm.html, 2021.
[34] NASA, Flying on mars is getting harder and harder - NASA mars, Retrieved July 20, 2024, from, https://mars.nasa.gov/technology/helicopter/status/334/flying-on-mars-is-getting-harder-and-harder/, 2021.
[35] E. Millour, F. Forget, A. Spiga, T. Pierron, A. Bierjon, L. Montabone, M. Vals, F. Lefèvre, J.-Y. Chaufray, M. Lopez-Valverde, F. Gonzalez-Galindo, S. Lewis, P. Read, M.-C. Desjean, F. Cipriani, the MCD Team, The mars climate database. Europlanet Science Congress, 2022, https://doi.org/10.5194/epsc2022-786. Granada, Spain, 18–23 Sep 2022, EPSC2022-786, Version 6.1.
[36] D. Raymer, Aircraft design: a conceptual approach, 6. AIAA Education Series, Reston, Va, 2018. Chaps. 20.11, 21.3.
[37] V. Youhanna, D. Ignatyev, L. Felicetti, Futuristic Martian aerobot design. UKRAS22 Conference “Robotics for Unconstrained Environments” Proceedings, 2022, pp. 64–65, https://doi.org/10.31256/Ec2Na5W.
[38] J. Gordon Leishman, Principles of Helicopter Aerodynamics, 2, Cambridge University Press, United Kingdom, 2006. Chaps. 2.15, 5.5.11.
[39] W. Johnson, Rotorcraft Aeromechanics, Cambridge University Press, 2013, https://doi.org/10.1017/CBO9781139235655. Chaps. 4.6, 5.3.
[40] Monolithic Power Systems.Web Editor, Introduction to battery technology: battery parameters, Monolithic Power Systems (2024). Retrieved December 18, 2024, from, https://www.monolithicpower.com/en/learning/mpscholar/battery-management-systems/introduction-to-battery-technology/battery-parameters.
[41] Jody Muelaner, Battery power tips, What to consider when evaluating battery performance. Battery Power Tips (2022). https://www.batterypowertips.com/what-to-consider-when-evaluating-battery-performance-faq/. (Accessed 18 December 2024).
[42] V. Youhanna, L. Felicetti, D. Ignatyev, Conceptual design study based on defined parameters for next generation Martian rotorcrafts, in: IEEE Aeroconf 2024, Montana, US, 2024, pp. 1–13, https://doi.org/10.1109/AERO58975.2024.10521441, 2-9 March 2024.
[43] V. Youhanna, L. Felicetti, D. Ignatyev, Parametric analysis of battery-electric rotorcraft configurations to fly on Mars, in: Aerospace Europe Conference Joint 10th EUCASS - 9th CEAS Conference 2023, 2023, https://doi.org/10.13009/EUCASS2023-319. Lausanne, 9-13 July 2023.
[44] E-One Moli Energy Corp, Product data sheet of INR-21700-P50B, Retrieved December 20, 2024, from, https://www.molicel.com/wp-content/uploads/Product-Data-Sheet-of-INR-21700-P50B-80122.pdf, 2024.
[45] V. Youhanna, L. Felicetti, D. Ignatyev, Preliminary design exploration of prospective multirotor aerobots, in: 34th Congress of the International Council of the Aeronautical Sciences (ICAS), 2024, 9-13 September 2024, Florence, Italy. Retrieved December 22, 2024, from, https://www.icas.org/ICAS_ARCHIVE/ICAS2024/data/preview/ICAS2024_0536.htm.
[46] K.M. Ferguson, D.G. Thomson, D. Anderson, M.L. Ireland, Z. Tu, S. Manso, A. B. Chandran, G. Ibal, Comparing the flight dynamics characteristics of tandem and conventional helicopters for the purposes of automatic control. Presented at the 41th European Rotorcraft Forum, 2015. Munich, Germany, September 1-4th, 2015. Retrieved December 22, 2024, from, https://dspace-erf.nlr.nl/server/api/core/bitstreams/a0eb3b54-7891-480a-b222-74360df252ac/content.

https://dspace.org/

Systematic methodology for the preliminary design of future rotary VTOL martian aerobots

Youhanna, Vishal; Felicetti, Leonard; Ignatyev, Dmitry

2025-06
Elsevier
https://doi.org/10.1016/j.actaastro.2025.01.059
Youhanna V, Felicetti L, Ignatyev D. (2025) Systematic methodology for the preliminary design of future rotary VTOL martian aerobots. Acta Astronautica, Volume 231, June 2025, pp. 246-267

Downloaded from a DSpace repository. https://dspace.org/